

CTCF and Cohesin Regulate Chromatin Loop Stability with Distinct Dynamics

Anders S. Hansen^{1,2}, Iryna Pustova^{1,2}, Claudia Cattoglio^{1,2}, Robert Tjian^{1,2*}, Xavier Darzacq^{1*}

¹Department of Molecular and Cell Biology, Li Ka Shing Center for Biomedical and Health Sciences, CIRM Center of Excellence, University of California, Berkeley, CA 94720, USA.

²Howard Hughes Medical Institute, Berkeley, CA 94720, USA.

*Correspondence to: jmlim@berkeley.edu (RT); darzacq@berkeley.edu (XD)

Abstract

Folding of mammalian genomes into spatial domains is critical for gene regulation. The insulator protein CTCF and cohesin control domain location by folding domains into loop structures, which are widely thought to be stable. Combining genomic and biochemical approaches we show that CTCF and cohesin co-occupy the same sites and physically interact as a biochemically stable complex. However, using single-molecule imaging we find that CTCF binds chromatin much more dynamically than cohesin ($\sim 1\text{-}2$ min *vs.* ~ 22 min residence time). Moreover, after unbinding, CTCF quickly rebinds another cognate site unlike cohesin for which the search process is long (~ 1 min *vs.* ~ 33 min). Thus, CTCF and cohesin form a rapidly exchanging “dynamic complex” rather than a typical stable complex. Since CTCF and cohesin are required for loop domain formation, our results suggest that chromatin loops are dynamic and constantly break and reform throughout the cell cycle.

INTRODUCTION

Mammalian interphase genomes are functionally compartmentalized into Topologically Associating Domains (TADs) spanning hundreds of kilobases. TADs are defined by frequent chromatin interactions within themselves and they are insulated from adjacent TADs (Dekker and Mirny, 2016; Dixon et al., 2012; Hu et al., 2015; Merkenschlager and Nora, 2016; Nora et al., 2012; Wang et al., 2016). Most TAD or domain boundaries are strongly enriched for CTCF (Figure 1A), an 11-zinc finger DNA binding protein (Ghirlando and Felsenfeld, 2016), and cohesin (Figure 1B), a ring-shaped multi-protein complex composed of Smc1, Smc3, Rad21 and SA1/2 that is thought to topologically entrap DNA (Ivanov and Nasmyth, 2005; Skibbens, 2016). The subset of TADs which are folded into loops are referred to as loop domains and tend to be demarcated by convergent CTCF binding sites (Rao et al., 2014). Targeted deletions of CTCF binding sites demonstrate that CTCF causally determines loop domain boundaries (Guo et al., 2015; Sanborn et al., 2015; de Wit et al., 2015). Moreover, disruption of loop domain boundaries by deletion or silencing of CTCF binding sites allows abnormal contact between previously separated enhancers and promoters, which can induce aberrant gene activation leading to cancer (Flavahan et al., 2015; Hnisz et al., 2016a) or developmental defects (Lupianez et al., 2015). Finally, genetically-engineered depletion of both CTCF (Nora et al., 2016) and cohesin (Schwarzer et al., 2016) causes most loops to disappear. Yet, despite much progress in characterizing TADs and loop domains, how they are formed and maintained remains unclear. Since CTCF and cohesin causally control domain organization, here we investigated their dynamics and nuclear organization using single-molecule imaging in live cells.

RESULTS

CTCF and cohesin form a loop maintenance complex

In order to image CTCF and cohesin without altering their endogenous expression levels, we used CRISPR/Cas9-mediated genome editing to homozygously tag *Ctcf* and *Rad21* with HaloTag in mouse embryonic stem (mES) cells (Figure 1C, clones C87 and C45). We also generated a double Halo-mCTCF/mRad21-SNAP_f knock-in mESC line (Figure 1C, C59) as well as a Halo-hCTCF knock-in human U2OS cell line (Figure 1C, C32). Halo- and SNAP_f-Tags can be covalently conjugated with bright cell-permeable small molecule dyes suitable for single-molecule imaging (Figure 1D; Figure 1–figure supplement 1; (Grimm et al., 2015)). To examine the effect of tagging CTCF and Rad21, which are both essential proteins, we performed control experiments in the doubly-tagged mESC line (C59), and observed no effect on mESC pluripotency in a teratoma assay (Figure 1–figure supplement 2),

expression of key stem cell genes (Figure 1–figure supplement 3A) or tagged protein abundance (Figure 1–figure supplement 3B). Next, to further validate our endogenous tagging approach we performed chromatin immunoprecipitation followed by DNA sequencing (ChIP-Seq) using antibodies against CTCF and Rad21 in both wild-type (wt) and the double knock-in C59 line. We compared ChIP-Seq enrichment for both wt and C59 at called wt peaks and observed similar enrichment (Figure 1E-F). Notably, 97% of the 33,434 called Rad21 peaks co-localize with one of the 68,077 called CTCF peaks (Figure 1–figure supplement 4-5; Supplementary File 1), suggesting an intrinsic link between CTCF and cohesin and largely confirming previous reports of ~70-90% overlap (Parelho et al., 2008; Wendt et al., 2008). However, chromatin co-occupancy by ChIP-seq at the same sites does not necessarily mean that CTCF and Rad21 bind simultaneously. Thus, to determine whether CTCF and cohesin physically interact, we performed co-immunoprecipitation (co-IP) studies. CTCF IP pulled down cohesin subunits Rad21, Smc1 and Smc3 in both wt and C59 mES cells (Figure 1G), demonstrating a physical interaction between CTCF and cohesin, which is not affected by endogenous tagging.

Together, our ChIP-Seq co-localization (97% of Rad21 peaks overlap with a CTCF peak) and co-IP interaction studies suggest that CTCF and cohesin form a complex on chromatin. The Hi-C study with the highest resolution found ~10,000 loops in human GM12878 cells using very conservative and stringent loop calling and found these loops to be largely conserved between cell types and between mouse and human (Rao et al., 2014). Since each loop is anchored by at least two CTCF/cohesin ChIP-Seq-called sites, but often by clusters of CTCF/cohesin sites, we estimate (see Supplementary File 2 for a full discussion) that at least one-third of cognate-bound CTCF molecules and the majority of chromatin-bound G1 cohesin molecules are involved in chromatin looping. Integrating these results with the recent demonstrations (Nora et al., 2016; Schwarzer et al., 2016) that CTCF and cohesin are causally required for chromatin looping, we refer to the subpopulation of CTCF and cohesin involved in looping as a “Loop Maintenance Complex” (LMC; Figure 1H).

CTCF and cohesin bind chromatin with very different dynamics

To investigate the dynamics of the LMC we measured the residence time of CTCF and cohesin on chromatin. First, we used highly inclined and laminated optical sheet illumination (Tokunaga et al., 2008) (Figure 2A) and single molecule tracking (SMT) to follow single Halo-CTCF molecules in live cells. By using long exposure times (500 ms), to “motion-blur” fast moving molecules into the background (Chen et al., 2014), we could visualize and track individual stable CTCF binding events (Figure 2B; Video 1). We recorded thousands of binding event trajectories and calculated their survival

probability. A double-exponential function, corresponding to specific and non-specific DNA binding (Chen et al., 2014), was necessary to fit the Halo-CTCF survival curve (Figure 2C). After correcting for photo-bleaching (Figure 2–Figure Supplement 1A), we estimated an average residence time (RT) of ~1 min for CTCF in mES cells and a slightly longer RT in U2OS cells (Figure 2D). DNA-binding defective CTCF mutants or Halo-3xNLS alone interacted very transiently with chromatin (RT ~1 s; Figure 2D). The measured RT did not depend on the dye or exposure time (Figure 2–figure supplement 1B). We note that a CTCF RT of ~1 min is a genomic average and that some binding sites likely exhibit a slightly longer or shorter mean residence time. We also note that there is likely an oversampling of binding events at CTCF binding sites showing the strongest ChIP-Seq enrichment (Figure 1E), which tend to be the sites involved in looping (Merkenschlager and Nora, 2016). To cross-validate these results using an orthogonal technique, we performed fluorescence recovery after photo-bleaching (FRAP) on Halo-CTCF and quantified the dynamics of recovery (Figure 2–figure supplement 2A-B). Both Halo-CTCF in mES cells (Figure 2E) and Halo-hCTCF in U2OS cells (Figure 2–figure supplement 2C) exhibited FRAP recoveries consistent with a RT ~ 1 min, but fitting the FRAP curves with a reaction-dominant model suggested a RT of 3-4 min (Figure 2–figure supplement 2D). Whereas our SMT measurements are limited by photobleaching, estimating RTs from FRAP modeling is more indirect and tends to significantly overestimate the RT of transcription factors (Mazza et al., 2012) and is also affected by anomalous diffusion. Therefore, we interpret 1 min as a lower bound and 4 min as an upper bound for CTCF’s RT in mESCs, but expect the true RT to be closer to 1 min than 4 min.

Our results differ considerably from a previous CTCF FRAP study using over-expressed transgenes, which reported rapid 80% recovery in 20 s (Nakahashi et al., 2013). However, when we used similar transiently over-expressed Halo-CTCF instead of endogenous knock-in cells, we also observed similarly rapid recovery (Figure 2–figure supplement 2B), suggesting that over-expression of target proteins can result in artefactual measurements. This finding underscores the importance of studying endogenously tagged and functional proteins. Thus, although CTCF (RT~1-2 min) binds chromatin much more stably than most sequence specific transcription factors (RT~2-15 s) (Chen et al., 2014; Mazza et al., 2012), its binding is still highly dynamic.

We next investigated the cell-cycle dependent cohesin binding dynamics (Gerlich et al., 2006). In addition to its role in holding together chromatin loops, cohesin mediates sister chromatid cohesion from replication in S-phase to mitosis. Thus, since TAD demarcation is strongest in G1 before S-phase (Naumova et al., 2013), we reasoned that cohesin dynamics in G1 should predominantly reflect the chromatin looping function of cohesin. To control for the cell-cycle, we deployed the Fucci system (Sakaue-Sawano et al., 2008) to distinguish G1 from S/G2-phase using fluorescent reporters in the C45

and C59 mESC lines (Figure 2–figure supplement 3A and 4). We then performed FRAP on mRad21-Halo (Figure 2F) and mRad21-SNAP_f (Figure 2–figure supplement 3B). We observed significantly faster mRad21 recovery in G1 than in S/G2-phase consistent with (Gerlich et al., 2006), but nevertheless much slower recovery than CTCF and CTCF showed the same recovery in G1 and S/G2 (Figure 2–figure supplement 2E). The slow mRad21 turnover precluded SMT experiments. Model-fitting of the G1 mRad21 FRAP curves (Figure 2–figure supplement 3C) revealed an RT~22 min. Previous cohesin FRAP studies have reported differing RTs (Gerlich et al., 2006; Huis in 't Veld et al., 2014) and as was seen for CTCF, over-expressed mRad21-Halo also showed much faster recovery than endogenous mRad21-Halo (Figure 2–figure supplement 3D). Although we cannot completely exclude a very small population (<5%) of CTCF or cohesin molecules with a somewhat shorter or longer RT, these RTs reflect chromatin-bound CTCF/cohesin. Since at least one-third of CTCF and the majority of G1 cohesin molecules bound to chromatin mediate looping (see Supplementary File 2 for estimate), we are confident that these RTs hold for most CTCF/cohesin molecules involved in looping.

Overall, while kinetic modeling of FRAP curves should be interpreted with some caution (Mazza et al., 2012), these results nevertheless demonstrate a surprisingly large (~10-20x) difference in RTs between CTCF and cohesin, which is difficult to reconcile with the notion of a biochemically stable LMC assembled on chromatin. However, although CTCF and cohesin do not form a stable complex on chromatin, it is still possible that CTCF and cohesin form a stable complex in solution when not bound to DNA.

CTCF and cohesin exhibit distinct nuclear search mechanisms

To investigate this possibility, we analyzed how CTCF and cohesin each explore the nucleus. Tracking fast-diffusing molecules has been a major challenge. To overcome this issue, we took advantage of bright new dyes (Grimm et al., 2016) and developed stroboscopic (Elf et al., 2007) photo-activation (Manley et al., 2008) single-molecule tracking (paSMT; Figure 3–figure supplement 1A), which makes tracking unambiguous (Materials and Methods). We tracked individual Halo-mCTCF molecules at ~225 Hz and plotted the displacements between frames (Figure 3A). Most Halo-mCTCF molecules exhibited displacements similar to our localization error (~35 nm; Materials and Methods) indicating chromatin association, whereas a DNA-binding defective CTCF mutant exhibited primarily long displacements consistent with free diffusion (Figure 3B; Video 2-3). To characterize the nuclear search mechanism, we performed kinetic modeling of the measured displacements (Figure 3–figure supplement 1B; Materials and Methods; (Mazza et al., 2012)) and found that in mES cells, ~49% of

CTCF is bound to cognate sites, ~19% is non-specifically associated with chromatin (e.g. 1D sliding or hopping) and ~32% is in free 3D diffusion (Table 1). Thus, after dissociation from a cognate site, CTCF searches for ~66 s on average before binding the next cognate site: ~65% of the total nuclear search is random 3D diffusion (~41 s on average), whereas ~35% (~25 s on average) consists of intermittent non-specific chromatin association (e.g. 1D sliding; Table 1; note this search time is based on a CTCF RT of ~1 min). The nuclear search mechanism of CTCF in human U2OS cells was similar albeit slightly less efficient (Table 1; Figure 3–figure supplement 1F). We note that CTCF's search mechanism, with similar amounts of 3D diffusion and 1D sliding, is close to optimal according to the theory of facilitated diffusion (Mirny et al., 2009).

Table 1.	Fraction bound (specific)	Fraction bound (non-specific)	Free 3D diffusion fraction	Apparent D_{FREE} ($\mu\text{m}^2/\text{s}$)	τ_{SEARCH} (total)	τ_{SEARCH} (free 3D diffusion)	τ_{SEARCH} (non-specific chromatin association)
mESC C59 Halo-mCTCF	48.9%	19.1%	32.0%	2.5	65.9 s	41.3 s	24.6 s
mESC C87 Halo-mCTCF	49.3%	19.1%	31.6%	2.3	62.6 s	39.0 s	23.6 s
U2OS C32 Halo-hCTCF	39.8%	17.7%	42.5%	2.5	102.8 s	71.9 s	30.9 s
mESC C45 mRad21-Halo: G1	39.8%	13.7%	46.5%	1.5	33.0 min	25.5 min	7.5 min
mESC C45 mRad21-Halo: S/G2	49.8%	13.7%	36.5%	1.5	n/a	n/a	n/a

Table 1. Nuclear search mechanism parameters. Table 1 lists key parameters for the nuclear search mechanism inferred from modeling fitting of the displacements in Figure 3 and the residence times in Figure 2.

Similar analysis of mRad21-Halo in G1 and S/G2 (Figure 3C-D) revealed that cohesin complexes diffuse rather slowly compared to CTCF (Table 1) and that roughly half of cohesins are topologically engaged with chromatin (G1: ~40%; S/G2: ~50%) compared to ~13% in non-specific, non-topological chromatin association and the remainder in 3D diffusion (G1: ~47%; S/G2: ~37%). Conversely, a Rad21 mutant (Haering et al., 2004) unable to form cohesin complexes displayed rapid diffusion and little chromatin association (Figure 3E). Like this Rad21 mutant, overexpressed wild-type mRad21-Halo also showed negligible chromatin association (Figure 3–figure supplement 1E) again underscoring the importance of studying endogenously tagged proteins at physiological concentrations. Importantly, this also shows that essentially all endogenously expressed mRad21-Halo is incorporated into cohesin complexes. Topological association and dissociation of cohesin is regulated by a complex interplay of co-factors such as Nipbl, Sororin and Wapl (Skibbens, 2016). If we nevertheless apply a simple two-state model to analyze cohesin dynamics (Materials and Methods), we estimate an average search time of ~33 min in between topological engagements of chromatin in G1, with ~77% of the total search time spent in 3D diffusion (~26 min) compared to ~23% in non-specific chromatin

association (7 min). Thus, for each specific topological cohesin chromatin binding-unbinding cycle in G1, CTCF binds and unbinds its cognate sites ~20-30 times. These results are certainly not consistent with a model wherein CTCF and cohesin form a stable LMC. Moreover, since CTCF diffuses much faster than cohesin (Table 1), it also seems unlikely that CTCF and cohesin form stable complexes in solution.

CTCF and cohesin co-localize in cells and show a clustered nuclear organization

To resolve these apparently paradoxical findings, we investigated the nuclear organization of CTCF and cohesin simultaneously in the same nucleus. We labeled Halo-mCTCF and mRad21-SNAP_f in C59 mES cells with the spectrally distinct dyes JF646 and JF549 (Grimm et al., 2015), respectively, and performed two-color direct stochastic optical reconstruction microscopy (dSTORM) super-resolution imaging in formaldehyde-fixed cells (Figure 4A). We localized individual CTCF and Rad21 molecules with a precision of ~20 nm, less than half the size of the cohesin ring. We observe significant clustering of both CTCF and Rad21 and a large fraction of these clusters overlap (Figure 4A and Figure 4—figure supplement 1A-C). We next confirmed clustering using photo-activation localization microscopy (PALM) and found that both CTCF and Rad21 predominantly form small clusters (Fig 4B and Figure 4—figure supplement 1; mean cluster radius ~30-40 nm). To determine whether individual CTCF and cohesin molecules co-localize, we calculated the pair cross correlation, $C(r)$ (Stone and Veatch, 2015). $C(r)$ quantifies spatial co-dependence as a function of length, r , and $C(r) = 1$ for all r under complete spatial randomness (CSR). CTCF and cohesin exhibited significant co-localization ($C(r) > 1$) at very short distances in mES cells (Figure 4C). Conversely, CTCF and cohesin were nearly independent at length scales beyond the diffraction limit, emphasizing the importance of super-resolution approaches. A mES cell line co-expressing histone H2B-SNAP_f and Halo proteins imaged under the same dSTORM conditions showed no pair cross-correlation (Figure 4C), thereby ruling out technical artifacts. Thus, our two-color dSTORM results provide compelling evidence that a large fraction of CTCF and cohesin molecules indeed co-localize at the single-molecule level inside the nucleus consistent with the LMC model and reveals a clustered nuclear organization.

DISCUSSION

Chromatin loop domains are widely believed to be very stable structures (Andrey et al., 2016; Ghirlando and Felsenfeld, 2016; Hnisz et al., 2016b) held together by a LMC composed of two CTCFs

and cohesin (whether cohesin acts as a single ring or as a pair of rings remains a matter of debate (Skibbens, 2016)). While our *in vitro* biochemical (Figure 1G) and co-localization (Figure 4A-C) experiments do demonstrate complex formation between CTCF and cohesin, our SMT experiments paradoxically reveal this complex to be highly transient and dynamic (Figure 2-3). To reconcile these observations, we therefore propose a “dynamic LMC” model. Consistent with previous studies, CTCF mainly functions to position cohesin at loop boundaries, whereas cohesin physically holds together the two chromatin strands. However, in the “dynamic LMC” model, while cohesin holds together a given chromatin loop, different CTCF molecules are frequently alighting and departing in a dynamic exchange thus giving rise to a “transient protein complex” with a molecular stoichiometry that cycles over time (Figure 4D). Since topological chromatin association of cohesin is infrequent (~33 min in G1), dissociation of cohesin (~22 min) likely causes the loop to fall apart (Figure 4D). Even if the CTCF and cohesin co-clusters that we observe (Figure 4A-C; Figure 4—figure supplement 1) are LMC clusters that hold together loop domains, their lifetimes are unlikely to be more than 1-2 hours. Thus, our results suggest that chromatin loops are continuously formed and dissolved throughout a typical 14-24 hour mammalian cell cycle.

Our results suggesting that loops are dynamic also provide experimental support for theoretical polymer simulation studies, which found that only dynamic, but not static, loop structures can reproduce experimentally observed chromatin interaction frequencies (Benedetti et al., 2014; Fudenberg et al., 2016; Giorgetti et al., 2014; Sanborn et al., 2015). We note that our quantitative characterization of CTCF and cohesin dynamics could be useful for parameterizing future polymer models. While our results indicate that loops are highly dynamic, the question of how they are formed remains. An attractive but not yet verified recent model suggests that loops are formed by cohesin-mediated loop extrusion (Fudenberg et al., 2016; Sanborn et al., 2015), whereby cohesin extrudes a loop by sliding on DNA (Davidson et al., 2016; Lengronne et al., 2004; Nasmyth, 2001; Stigler et al., 2016) until it encounters two convergent and bound CTCF sites (Figure 4E). Our imaging experiments (Figure 2-3) cannot readily distinguish cohesin stably bound at loop anchors from cohesin in the process of extrusion and thus our measured residence time of ~22 min reflects the average total duration of both. In the context of the loop extrusion model, our results suggest a mechanism for boundary permeability through dynamic and stochastic CTCF occupancy at cognate CTCF sites, which may explain the formation of competing loop domains (Figure 4E). This would also explain why DNA-FISH measurements show that most loops are only present in a subset of cells at any given time (Sanborn et al., 2015; Williamson et al., 2014). Finally, the highly dynamic view of frequently breaking and forming

241 chromatin loops presented here may also facilitate dynamic long-distance enhancer-promoter scanning
242 of DNA in *cis*, which may be important for temporally efficient regulation of gene expression.

FIGURE LEGENDS

Figure 1. CTCF and cohesin can be endogenously tagged and form a complex. (A) Sketch of CTCF and its consensus DNA binding sequence. (B) Sketch of cohesin, with subunits labeled, topologically entrapping DNA. (C) Western blot of mESC and U2OS wild-type (wt) and knock-in cell lines demonstrating homozygous insertions. (D) Sketch of covalent dye-conjugation for Halo or SNAP_f-Tag. (E) CTCF ChIP-Seq read count (Reads Per Genomic Content) for wild-type and C59 plotted at MAC2-called wt-CTCF peak regions centered around the peak. (F) Rad21 ChIP-Seq read count (Reads Per Genomic Content) for wild-type and C59 plotted at MACS2-called wt-Rad21 peak regions. (G) Co-IP. CTCF was immunoprecipitated and we immunoblotted for cohesin subunits Rad21, Smc1 and Smc3. (H) Sketch of a Loop Maintenance Complex (LMC) composed of CTCF and cohesin holding together a spatial domain as a loop.

Figure Supplement 1. Specific labeling of HaloTagged and SNAP_f-tagged proteins in live cells.

Figure Supplement 2. Teratoma assay demonstrates that tagging CTCF and Rad21 does not affect pluripotency in mESCs

Figure Supplement 3. Tagging CTCF and Rad21 does not affect expression of key pluripotency genes or CTCF and Rad21 protein levels

Figure Supplement 4. CTCF and Rad21 ChIP-Seq results in wt and C59 mESCs

Figure Supplement 5. Tagging CTCF and Rad21 does not affect the ChIP-Seq genomic binding pattern

Figure 2. CTCF and cohesin have very different residence times on chromatin. (A) Sketch illustrating HiLo (highly inclined and laminated optical sheet illumination) (Tokunaga et al., 2008). (B) Example images showing single Halo-mCTCF molecules labeled with JF549 binding chromatin in a live mES cell. (C) A plot of the uncorrected survival probability of single Halo-mCTCF molecules and one- and two-exponential fits. Right inset: a log-log survival curve. (D) Photobleaching-corrected residence times for Halo-CTCF, Halo-3xNLS and a zinc-finger (11 His→Arg point-mutations) mutant or entire deletion of the zinc-finger domain. Error bars show standard deviation between replicates. For each replicate we recorded movies from ~6 cells and calculated the average residence time using H2B-Halo for photobleaching correction. Each movie lasted 20 min with continuous low-intensity 561 nm excitation and 500 ms camera integration time. Cells were labeled with 1-100 pM JF549. (E) FRAP recovery curves for Halo-mCTCF, H2B-Halo and Halo-3xNLS in mES cells labeled with 1 μM Halo-TMR. (F) FRAP recovery curves for mRad21-Halo and H2B-Halo in mES cells labeled with 1 μM Halo-TMR. Right: sketch of Fucci cell-cycle phase reporter (Sakaue-Sawano et al., 2008; Sladitschek and Neveu, 2015). We modified the system to contain mCitrine-hGem(aa1-110) and SFCP3A-hCdt(aa30-120) to avoid overlap in the red region of the electromagnetic spectrum. Each FRAP curve shows mean recovery from >15 cells from ≥3 replicates and error bars show the standard error.

Figure Supplement 1. Illustration of how residence times are inferred from SMT and control experiments

Figure Supplement 2. Supplementary and control CTCF FRAP experiments

Figure Supplement 3. Supplementary and control cohesin FRAP experiments

Figure Supplement 4. Validation of Fucci Reporters.

Figure 3. Dynamics of CTCF and cohesin's nuclear search mechanism. Single-molecule displacements from ~225 Hz stroboscopic (single 1 ms 633 nm laser pulse per camera integration event) paSMT experiments over multiple time scales for (A) C59 Halo-mCTCF, (B) a Halo-mCTCF mutant with the zinc-finger domain deleted, C45 mRad21-Halo in S/G2 phase (C) and G1 phase (D) and (E) a Rad21 mutant that cannot form cohesin complexes. Kinetic model fits (3 fitted parameters) to raw displacement histograms are shown as black lines. All calculated and fitted parameters are listed in Table 1. Displacement histograms were obtained by merging data from at least 24 cells from at least 3 replicates

Figure Supplement 1. Supplementary stroboscopic paSMT experiments and controls

Figure 4. Models of CTCF/cohesin mediated chromatin loop dynamics. (A) Two-color dSTORM of C59 mESCs with mRad21-SNAP_f labeled with 500 nM JF549 (green) and Halo-mCTCF labeled with 500 nM JF646 (magenta). High-intensity co-localization is shown as white. Low intensity co-localization is not visible. Zoom-in on red 3 μm square. Note, the SNAP dye cp-JF549 shows slight artefactual labeling of the nuclear envelope, which was removed during image rendering. (B) Cluster radii distributions for CTCF (C87 and C59) and Rad21 (C45) from single-color PALM experiments using PA-JF549 dyes. (C) Pair cross correlation of C59 and mESC H2B-SNAP_f co-expressing Halo-only. Error bars are standard error from 12-18 dSTORM-

imaged cells over three replicates. **(D)** Sketch illustrating the concept of a dynamic Loop Maintenance Complex (LMC) composed of CTCF and cohesin with frequent CTCF exchange and slow, rare cohesin dissociation, which causes loop deformation and topological re-orientation of chromatin. **(E)** Sketch illustrating how dynamic CTCF exchange during loop extrusion of cohesin may explain alternative loop formations when two competing convergent sites (B and C) for another site (A) exist.

Figure Supplement 1. Overview of super-resolution PALM approach and control experiments.

Legends for Videos

Video 1

Single-molecule tracking of Halo-mCTCF in mESCs at 2 Hz. Related to Figure 2. Using long 500 ms camera integration causes most diffusing molecules to “motion-blur” into the background. Laser: 561 nm. Dye: JF549. One pixel: 160 nm.

Video 2

Single-molecule tracking of Halo-mCTCF in mESCs at 225 Hz. Related to Figure 3. Stroboscopic (1 ms of 633 nm) paSMT allows tracking of fast-diffusing molecules. Lasers: 405 and 633 nm. Dye: PA-JF646. One pixel: 160 nm.

Video 3

Single-molecule tracking of Δ ZF-Halo-mCTCF in transiently transfected mESCs at 225 Hz. Related to Figure 3. Stroboscopic (1 ms of 633 nm) paSMT allows tracking of fast-diffusing molecules. Lasers: 405 and 633 nm. Dye: PA-JF646. One pixel: 160 nm.

Acknowledgements

We thank Luke Lavis for generously providing JF dyes, Gina M. Dailey for extensive assistance with cloning, Astou Tangara for microscopy assembly and maintenance, and Dr. Kartoosh Heydari at the Li Ka Shing Facility for flow cytometry assistance. We thank Sheila Teves and other members of the Tjian and Darzacq labs, Douglas Koshland, Miriam Huntley, James Rhodes and Kim Nasmyth, and Leonid Mirny and other 4D Nucleome consortium members for insightful comments on the manuscript. This work was performed in part at the CRL Molecular Imaging Center, supported by the Gordon and Betty Moore Foundation. This work used the Vincent J. Coates Genomics Sequencing Laboratory at UC Berkeley, supported by NIH S10 Instrumentation Grants 10RR029668 and S10RR027303. ASH is a postdoctoral fellow of the Siebel Stem Cell Institute. This work was supported by NIH grants U01-EB021236 and U54-DK107980 (XD), the California Institute of Regenerative Medicine grant LA1-08013 (XD), and by the Howard Hughes Medical Institute (003061, RT). ChIP-Seq data has been deposited at NCBI GEO under accession code GSE90994 and is available at:

<https://www.ncbi.nlm.nih.gov/geo/query/acc.cgi?token=mfmreiekfhatjql&acc=GSE90994>

Competing interests

RT: member of eLife’s Board of Directors. The other authors declare that no competing interests exist.

Additional Files

Supplementary File 1: Table with ChIP-Seq relevant information.

338 Supplementary File 2: Supplementary information and table with primer sequences.
339 Video 1-3.
340

Legends for Figure Supplements

Figure 1–Figure Supplement 1.

Specific labeling of HaloTagged and SNAP_F-Tagged proteins in live cells.

Wild-type (wt) mouse embryonic stem cells (mESCs) and C59 mESCs expressing endogenously tagged FLAG-Halo-mCTCF and mRad21-SNAP_F-V5 were labelled with the indicated dye by 30 min incubation in a 37°C incubator followed by washing with PBS and fresh medium, preparation for FACS (dissociation with trypsin, cell collection by centrifugation and filtering through 40 µm mesh) and their fluorescence was then measured using analytical flow cytometry. Around 30,000 cells were measured in each case and live cells were gated using the area of forward and side scattering. JF549/TMR fluorescence was measured using a 561 nm excitation laser and a 610/20 nm emission filter. JF646 fluorescence was measured using a 640 nm excitation laser and a 670/30 nm emission filter. Each panel shows fluorescence in the JF549/TMR channel and in the JF646 channel as well as a JF549/TMR vs. JF646 scatterplot. First panel: no dye control. Second panel: 500 nM SNAP-TMR (NEB #S9105S) labeling only. Third panel: 500 nM cp-JF549 labeling only (the cp handle also labels SNAP_F-Tag proteins, but more specifically than the SNAP-handle). Fourth panel: 500 nM Halo-JF549 labeling only. Fifth panel: 500 nM Halo-JF646 labeling only. Bottom panel: double 500 nM cp-JF549 and 500 nM Halo-JF646 labeling.

Figure 1–Figure Supplement 2.

Teratoma assay demonstrates that tagging CTCF and Rad21 does not affect pluripotency in mESCs

350,000 wild-type and C59 (FLAG-Halo-mCTCF; mRad21-SNAP_F-V5) JM8.N4 mouse embryonic stem cells were injected into the testis and kidney of Fox Chase SCID-beige male 8 week old mice (Charles River) and tumors were harvested 27-33 days after injection (top row). Tumors were fixed with 10% formalin overnight, embedded in paraffin and cut into 5 µm serial sections and then H&E stained. Representative sections from each of the three germ layers (endoderm, mesoderm and ectoderm; highlighted by black arrows) are shown for both wild-type and C59 mES cells. Black scale bar: 100 µm.

Figure 1–Figure Supplement 3.

Tagging CTCF and Rad21 does not affect expression of key pluripotency genes or CTCF and Rad21 protein levels

(A) Expression of key mouse embryonic stem cell genes measured by qPCR was similar in wild-type (blue) and C59 (FLAG-Halo-mCTCF; mRad21-SNAP_F-V5) (red) JM8.N4 mouse embryonic stem cells. (B) CTCF (red) and Rad21 (green) protein levels as measured by western blot and normalized to either H3 levels (solid bar) or TBP (hashed bar) was similar between wild-type and tagged mouse embryonic stem cells (WT, C87, C45, C59) and similar between wild-type and tagged human U2OS cells (WT, C32). Error bars show standard deviation among three replicates.

Figure 1–Figure Supplement 4.

CTCF and Rad21 ChIP-Seq results in wt and C59 mESCs

(A) Venn Diagram showing overlap of called peaks (MACS2) of CTCF and Rad21 in wild-type mESCs. (B) Representative genome-browser view of IgG, CTCF and Rad21 ChIP-Seq for wild type (wt) and the double knock-in C59 mES cells at the Nanog locus on chromosome 6. As can be seen, the binding pattern of both CTCF and Rad21 is unaltered after tagging. Scale is (number of reads)/(10⁶/(total read count)). (C) Representative genome-browser view of IgG, CTCF and Rad21 ChIP-Seq for wild type (wt) and the double knock-in C59 mES cells at the Oct4 (Pou5f1) locus on chromosome 17. As can be seen, the binding pattern of both CTCF and Rad21 is unaltered after tagging. Scale is (number of reads)/(10⁶/(total read count)).

Figure 1–Figure Supplement 5.

Tagging CTCF and Rad21 does not affect the ChIP-Seq genomic binding pattern

(A) ChIP-Seq enrichment (RPGC: Reads Per Genomic Content) shown for all called CTCF peaks in wild-type mESCs, sorted by wild-type CTCF enrichment. The 6 columns show IgG ChIP-Seq, CTCF ChIP-Seq and mRad21 ChIP-Seq for wild-type (left) and C59 (FLAG-Halo-mCTCF; mRad21-SNAP_r-V5) genome-edited (right) cells. On the right, the average in each case for the same conditions. (B) ChIP-Seq enrichment (RPGC: Reads Per Genomic Content) shown for all called Rad21 peaks in wild-type mESCs, sorted by wild-type Rad21 enrichment. The 6 columns show IgG ChIP-Seq, CTCF ChIP-Seq and mRad21 ChIP-Seq for wild-type (left) and C59 (FLAG-Halo-mCTCF; mRad21-SNAP_r-V5) genome-edited (right) cells. On the right, the average in each case for the same conditions.

Figure 2–Figure Supplement 1.

Illustration of how residence times are inferred from SMT and control experiments

(A) Illustration of how residence times were inferred from single-molecule tracking experiments. Left, a double-exponential fit to Halo-CTCF and H2B-Halo survival curves measured from the two cell lines on the same day. H2B-Halo shows negligible turnover within the observation time window and thus the measured off-rate for H2B-Halo was taken as the rate of photo-bleaching. Right, a sketch showing the inferred residence time (true CTCF off rate = measured CTCF off rate - measured H2B off rate) as a function of the frame threshold used for the two-exponential fitting. The residence time was taken as the inferred residence time once convergence was reached (threshold=2.5 seconds). (B) Bar graph showing that the CTCF residence time does not depend on the exposure time or dye used. Left, C87 Halo-mCTCF was labeled with JF549 and residence time was measured as in (A) using exposure times of either 300 ms, 500 ms or 800 ms. Right, residence time was measured as in (A) using an exposure time of 500 ms with C87 Halo-mCTCF and HaloTag dyes TMR, JF549 and JF646. Error bars show the standard deviation between replicates – each replicate consisted of 20 min movies of ~6 cells corrected for photobleaching using a similar number of H2B-Halo cells labelled with the same dye and using the same exposure time. At least three replicates were performed.

Figure 2–Figure Supplement 2.

Supplementary and control CTCF FRAP experiments

(A) Representative raw confocal microscopy images of H2B-Halo, C59 Halo-mCTCF and C32 Halo-hCTCF each labeled with 1 μ M TMR just before, 1 s after, 10 s after and 4 min after bleaching a 1 μ m circular spot (green circle). mES cells especially show significant movement on the minute time-scale and all movies were drift-corrected. (B) Photo-bleaching corrected FRAP curves measured at one frame per second in mESCs. C59 and C87 Halo-mCTCF show the behavior of endogenously-tagged CTCF, and transiently transfected Halo-mCTCF expressed from a CMV-promoter is shown in black. As can be clearly seen, the CTCF FRAP recovery is much faster when overexpressed. Error bars show standard error. (C) Photobleaching corrected FRAP curves measured at one frame per second in human U2OS cells. Halo-3xNLS and H2B-Halo are controls for rapid and negligible recovery, respectively, demonstrating the validity our photobleaching- and drift-correction approaches. CTCF recovery in human U2OS cells is similar, albeit slightly slower than in mESCs. (D) Model-fitting of C87 and C59 Halo-mCTCF FRAP curves using a reaction dominant model (Materials and Methods) for FRAP experiments at either 11 min and 0.5 Hz or 5 min and 1 Hz. The model-inferred residence time and the 95% confidence interval (CI) from the fitting is shown. (E) Dynamics of Halo-mCTCF (C59 mESCs) does not change with between G1- and S/G2-phase of the cell cycle. G1 and S/G2 were distinguished using the Fucci system (Figure 2–Figure Supplement 4).

Figure 2–Figure Supplement 3.

Supplementary and control cohesin FRAP experiments

(A) Top, sketch of the Fucci-system, which distinguishes cells in G1-phase from S/G2-phase of the cell cycle. Bottom, representative raw confocal microscopy images of mESC C45 mRad21-Halo in G1 or S/G2 labeled with 1 μ M TMR just before, 2 s after, 2 min after and 10 min after bleaching a 1 μ m circular spot (green circle). We corrected for cell drift. (B) FRAP curves for SNAP_f-tagged mRad21 (C59 mRad21-SNAP_f-V5) similar to FRAP curves for C45 presented in main figure 2F. C59 mRad21-SNAP_f co-expressing Fucci reporters or H2B-SNAP_f mESCs were labeled with cp-JF549, a small molecule dye that specifically labels the SNAP_f but not the Halo-Tag, and FRAP recovery measured, photobleaching and drift-corrected. Overall, the FRAP recovery of mRad21-Halo and mRad21-SNAP_f were identical within error. Error bars show standard error. (C) show exponential-model fits (black line) to C45 mRad21-Halo and C59 mRad21-SNAP_f FRAP curves (blue data) in G1-phase of the cell cycle. We stress that while direct modeling of FRAP curves suffers from fitting models with several fitted parameters to relatively simply data curves, a rough residence time estimate can nevertheless be obtained. The average inferred residence time and 95% confidence intervals (CI) are shown. (D) FRAP of endogenous and transiently transfected mRad21-Halo in interphase cells. For C45 mRad21-Halo we “simulated” interphase cells by scaling the G1 to S/G2 FRAP by 1:7 (roughly the ratio of G1 to S/G2 cells for mESCs). For transient transfections, wild-type mESCs were transfected with a plasmid encoding either pCMV-mRad21-Halo (high expression) or pL30-mRad21-Halo (lower expression). Cells were transfected with Lipofectamine 3000 using the ThermoFisher Scientific protocol the day before the FRAP imaging. On the imaging day, cells were labeled with 1 μ M TMR. Error bars show standard error. (E) Radial bleach spot profile. The radial bleach spot profile was determined by calculating the FRAP recovery at the perimeter of circles of increasing radii in increments of 100 nm. This was averaged over multiple cells (~20-30 cells). Curves show the mean radial profile along with the standard deviation (error bars) for C59 Halo-mCTCF, C45 mRad21-Halo in G1 and mESC H2B-Halo. As can be seen, diffusion does not significantly affect the recovery at a radius of 0.6 μ m, which is what

we used for calculating the FRAP recovery. **(F)** FRAP recovery for H2B-SNAPf labeled with 500 nM cp-JF549, extensively washed and then with or without blocking with 500 nM SNAP-block (a “dark” ligand). As can be seen there was no effect on the FRAP recovery within error (error bars show standard error). Thus, re-binding of insufficiently washed out dye after the bleach pulse does not significantly affect our FRAP recovery at the time-scales we are working at.

Figure 2–Figure Supplement 4.

Validation of Fucci Reporters

(A) FACS gating of C59 mESCs co-expression the Fucci reporters mCherry-hCdt(aa30-120) and mCitrine-hGem(aa1-110) with the four polygon gates shown (Sakaue-Sawano et al., 2008; Sladitschek and Neveu, 2015). Cells in G1 express mCherry-hCdt(aa30-120) but not mCitrine-hGem(aa1-110), whereas cells in S/G2 express mCitrine-hGem(aa1-110) but not mCherry-hCdt(aa30-120). For FRAP and SMT experiments where small-molecule dyes in the red part of the electromagnetic spectrum were used (TMR, JF549 or JF6464), we used SCFP3A-hCdt instead of mCherry-hCdt. We also note that strictly speaking, only the mCitrine-hGem(aa1-110) reporter is necessary since cells negative for this reporter must be in G1. **(B–E)** histograms showing DAPI (which stains DNA) signal for the gated populations in **(A)**. Cells in G1 have not replicated their DNA and thus have 2n chromosomes **(D)**, whereas cells in G2 have finished replicating their DNA and have 4n chromosomes. Cells in S-phase are actively replicating DNA and have an intermediate number of chromosomes **(E)**. As can be seen, the Fucci system allows us to enrich for a relatively pure G1 population **(D)**.

Figure 3–Figure Supplement 1.

Supplementary stroboscopic paSMT experiments and controls

(A) Sketch illustrating stroboscopic paSMT. Sketch illustrating labeling Halo-tagged proteins, e.g. CTCF or Rad21, with PA-JF646. This dye remains dark until 405 nm activation, which converts it to regular fluorescent JF646. The advantage is that thousands of single-molecule trajectories can be recorded from a single cell at a density of ~ 0.5 fluorescent molecules per nucleus, which makes tracking unambiguous, by using very low 405 nm excitation. Since high 633 nm laser powers are used, most molecules bleach within 5-10 frames. We use PA-JF646 instead of PA-JF549 since the red-shifted 633 nm laser induces less photo-toxicity, although the displacement histograms were identical between PA-JF549 and PA-JF646. Moreover, we never record for more than 2 min per cell. We observed no visible signs of photo-toxicity after 2 min of paSMT. Below, sketch illustrating stroboscopic illumination. To minimize “motion-blurring” of fast-diffusing molecules, we used pulsed 633 nm excitation with 1 ms pulses. The camera integration time was 4 ms + ~ 0.447 ms (frame-transfer mode) resulting in a frame rate of roughly 225 Hz. Below, raw microscopy images demonstrating that even fast-diffusing molecules can be imaged and tracked (red lines) at high signal-to-background. **(B)** Overview of 2-state dynamic displacement model. Full details are provided in the materials and methods. Briefly, the model assumes molecules can exist in either a chromatin associating (specific and non-specific) state called “bound” or in a free 3D diffusion state called “free”. A mathematical model describing how the distribution of displacements, r , depends on the time delay, fraction bound, diffusion constants, localization error and axial detection slice is shown below. Overall, the model contains 3 fitted parameters, which were estimated using least squares fitting to the raw displacements considering the first seven displacements ($\Delta\tau \sim 4.5$ ms to 31.5 ms). For ease of visualization, we show displacement histograms in **(C–F)**, but the fitting was performed on cumulative distribution functions (CDFs) to minimize binning artifacts. **(C–F)** displacement histograms for various cell lines all measured using the

approach in (A-B). For ease of visualization the displacement histograms are cut off at 1050 nm, but longer trajectories were included in the model fitting. (C) shows Halo-only and Halo-3xNLS in mESCs, which show negligible binding. Note, that most fast-diffusing molecules eventually move out of the focal plane. (D) shows various Halo-mCTCF constructs. C59 and C87 are endogenous Halo-mCTCF knock-ins. pL30-wt-Halo-mCTCF was transiently expressed using a weak promoter (L30). Compared to Halo-mCTCF overexpressed by the strong CMV promoter, overexpressing Halo-mCTCF using a weak promoter (L30) causes only a minor (10 percentage points; likely due to saturation of binding sites) underestimation of the fraction bound. Right, two transiently transfected Halo-mCTCF mutants: 11ZF-mut-Halo-mCTCF is a CTCF mutant with an essential His amino acid in all 11 zinc-fingers mutated to Arg, which should abolish specific DNA-binding. We used this mutant to estimate the non-specifically bound fraction. Δ ZF-Halo-mCTCF has the entire 11-zinc-finger domain deleted. We used this mutant to verify that the zinc-finger domain solely is responsible for chromatin association. (E) H2B-Halo and Rad21 experiments in mESCs. We used H2B-halo as a control for a protein that is almost exclusively bound. Note that since we use an EF1a promoter to express H2B, which is not cell-cycle regulated, some H2B-molecules do show free diffusion. mRad21-Halo in S/G2 and G1 are also shown, as is transiently transfected wt-mRad21-Halo expressed using the low-expression promoter, L30. Even though mRad21-Halo is only weakly overexpressed, most molecules show free 3D diffusion. The overexpression artifact may be caused by the fact that without similar overexpression of Smc1, Smc3 and SA1/2, most Rad21 cannot form cohesin complexes. Finally, a Rad21-mutant (F601R, L605R, Q617K), which cannot form cohesin complexes was used to estimate the non-specifically bound Rad21 fractions. (F) Stroboscopic paSMT experiments in human U2OS cells. H2B-Halo and Halo-3xNLS were used as controls for mostly bound and free molecules and the same zinc-finger mutants as in mESCs were transiently transfected as control for non-specific chromatin association. Note that C32 Halo-hCTCF shows slightly more free diffusion than C59 and C87 in mESCs.

Figure 4–Figure Supplement 1.

Overview of super-resolution PALM approach and control experiments

(A) Representative super-resolution PALM reconstruction of Halo-mCTCF in C59 mouse embryonic stem cells. Left: full nucleus. Right: zoom-in on a 3 μ m square before (top) and after (bottom) cluster assignment using a Bayesian clustering algorithm. (B) Representative super-resolution PALM reconstruction of mRad21-Halo in C45 mouse embryonic stem cells. Left: full nucleus. Right: zoom-in on a 3 μ m square before (top) and after (bottom) cluster assignment using a Bayesian clustering algorithm. (C) Bar graphs showing fraction of molecules in clusters for different mES cell lines as inferred from Bayesian cluster assignments. Bar graphs show mean per 3 μ m square and the error bars show the standard error. (D) Bar graphs showing cluster radii in clusters for different mES cell lines as inferred from Bayesian cluster assignments. Bar graphs show mean per 3 μ m square and the error bars show the standard error. (E) Representative control for photo-blinking in apparent PALM clustering. U2OS C32 Halo-hCTCF was labeled with ~50:50 PA-JF549:PA-JF646 and imaged using two-color PALM. Clusters were assigned as in (C-D) and the fraction of CTCF molecules in each cluster labeled with JF549 and JF646 plotted. If PALM clustering was solely a photo-blinking artifact, clusters should be exclusively composed of either JF549 or JF646, whereas under ideal conditions the distribution should follow a binomial distribution. The observed distributions resemble the expected binomial distributions suggesting that most called clusters are not a photo-blinking artifact (Kullback-Leibler divergence ~ 0.3 bits).

Materials and Methods

Cell culture, stable cell line construction and dye labeling

JM8.N4 mouse embryonic stem cells (Pettitt et al., 2009) (Research Resource Identifier: RRID:CVCL_J962; obtained from the KOMP Repository at UC Davis) were grown on plates pre-coated with a 0.1% autoclaved gelatin solution (Sigma-Aldrich, G9391) under feeder free condition in knock-out DMEM with 15% FBS and LIF (full recipe: 500 mL knockout DMEM (ThermoFisher #10829018), 6 mL MEM NEAA (ThermoFisher #11140050), 6 mL GlutaMax (ThermoFisher #35050061), 5 mL Penicillin-streptomycin (ThermoFisher #15140122), 4.6 μ L 2-mercapoethanol (Sigma-Aldrich M3148), 90 mL fetal bovine serum (HyClone FBS SH30910.03 lot #AXJ47554)) and LIF. mES cells were fed by replacing half the medium with fresh medium daily and passaged every two days by trypsinization. Human U2OS osteosarcoma cells (Research Resource Identifier: RRID:CVCL_0042; a gift from David Spector's lab, Cold Spring Harbor Laboratory) were grown in low glucose DMEM with 10% FBS (full recipe: 500 mL DMEM (ThermoFisher #10567014), 50 mL fetal bovine serum (HyClone FBS SH30910.03 lot #AXJ47554) and 5 mL Penicillin-streptomycin (ThermoFisher #15140122)) and were passaged every 2-4 days before reaching confluency. For live-cell imaging, the medium was identical except DMEM without phenol red was used (ThermoFisher #31053028). Both mouse ES and human U2OS cells were grown in a Sanyo copper alloy IncuSafe humidified incubator (MCO-18AIC(UV)) at 37°C/5.5% CO₂.

For all single-molecule experiments (both live and fixed), cells were grown overnight on 25 mm circular no 1.5H cover glasses (Marienfeld High-Precision 0117650). Prior to all experiments, the cover glasses were plasma-cleaned and then stored in isopropanol until use. For U2OS cell lines, cells were grown directly on the cover glasses and for mouse ES cells, the cover glasses were coated with Corning Matrigel matrix (Corning #354277; purchased from Fisher Scientific #08-774-552) according to manufacturer's instructions just prior to cell plating. After overnight growth, cells were labeled with the relevant Halo- or SNAP-dye at the indicated concentration for 15 min (Halo) or 30 min (SNAP) and washed twice (one wash: medium removed; PBS wash; replenished with fresh medium). At the end of the final wash, the medium was changed to phenol red-free medium keeping all other aspects of the medium the same.

For FRAP experiment, cell preparation was identical except cells were grown on glass-bottom (thickness #1.5) 35 mm dishes (MatTak P35G-1.5-14-C), either directly (U2OS) or Matrigel coated (mESC).

Mouse ES cell lines stably expressing H2B-Halo, H2B-SNAPf, Fucci reporters or Halo-3xNLS were generated using PiggyBac transposition and drug selection. Briefly, the relevant gene (e.g. H2B-Halo) was cloned into a PiggyBac vector co-expressing a drug resistance gene (G418 or Puromycin) and this vector was then co-transfected together with a SuperPiggyBac transposase vector into the relevant mouse ES cell line using Lipofectamine 3000 according to manufacturer's instructions (2 μ g expression vector and 1 μ g PiggyBac transposase vector per well in a 6-well plate). The following day, selection was then started by adding 1 mg/mL G418 or 5 μ g/mL puromycin. An untransfected cell line was selected in parallel and selection was judged to be complete once no live cells were left in the untransfected cell line. For human U2OS cells, stable cell lines were generated by random integration by transfecting the relevant expression vector with drug selection without using the PiggyBac system. Selection was performed in the same way as for mouse ES cells.

CRISPR/Cas9-mediated genome editing

Knock-in cell lines were created roughly according to published procedures (Ran et al., 2013), but exploiting the HaloTag and SNAP_f-Tag to FACS for edited cells. The SNAP_f-Tag is an optimized version of the SNAP-Tag and we purchased a plasmid encoding this gene from NEB (NEB #N9183S). We transfected both U2OS and mES cells using Lipofectamine 3000 (ThermoFisher L3000015) according to manufacturer's protocol, co-transfecting a Cas9 and a repair plasmid (2 μ g repair vector

and 1 µg Cas9 vector per well in a 6-well plate; 1:2 w/w). The Cas9 plasmid was slightly modified from that distributed from the Zhang lab (Ran et al., 2013): 3xFLAG-SV40NLS-pSpCas9 was expressed from a CBh promoter; the sgRNA was expressed from a U6 promoter; and mVenus was expressed from a PGK promoter. For the repair vector, we modified a pUC57 plasmid to contain the tag of interest (e.g. Halo or SNAP_f) flanked by ~500 bp of genomic homology sequence on either side. For N-terminal FLAG-Halo-tagging of mouse *Ctcf* and human *CTCF*, we introduced synonymous mutations (mCTCF: first 9 codons after ATG; hCTCF: first 12 codons after ATG), where possible, to prevent the Cas9-sgRNA complex from cutting the repair vector. For C-terminal tagging of mouse *Rad21* with SNAP_f-V5, this was not possible. Instead we designed sgRNAs that overlapped with the STOP codon and, thus, that would not cut the repair vector. For Halo-hCTCF and Halo-mCTCF we used a TEV linker sequence (EDLYFQS) to link the Halo protein to CTCF; for mRad21 we used the Sheff & Thorn linker (GDGAGLIN) (Sheff and Thorn, 2004).

In each case we designed 3 or 4 sgRNAs using the Zhang lab CRISPR design tool (<http://tools.genome-engineering.org>), cloned them into the Cas9 plasmid and co-transfected each sgRNA-plasmid with the repair vector individually. 18-24 h later, we then pooled cells transfected with each of the sgRNAs individually and FACS-sorted for YFP (mVenus) positive, successfully transfected cells. YFP-sorted cells were then grown for 4-12 days, labelled with 500 nM Halo-TMR (Halo-Tag knock-ins) or 500 nM SNAP-JF646 (SNAP_f-Tag knock-in) and the cell population with significantly higher fluorescence than similarly labelled wild-type cells, FACS-selected and plated at very low density (~0.1 cells per mm²; mES cells) or sorted individually into 96-well plates (U2OS cells). Clones were then expanded and genotyped by PCR using 3-primer PCR (genomic primers external to the homology sequence and an internal Halo or SNAP_f primer). Successfully edited clones were further verified by PCR with multiple primer combinations, Sanger sequencing and Western blotting. We isolated ~6-10 homozygous knock-in clones for each line. The clones chosen for further study all showed similar tagged protein levels to the endogenous untagged protein in wild-type controls.

Sequences for primers and sgRNAs are given in Supplementary File 2. All plasmids used in this study, including for genome-editing and transient transfections, are available upon request.

Teratoma assays

To verify that genome-edited mES cell lines remain pluripotent, we performed teratoma assays and compared wild-type and C59 FLAG-Halo-mCTCF; mRad21-SNAP_f-V5 knock-in cells. Briefly, 350,000 cells were injected into the kidney capsule and testis of two 8-week old Fox Chase SCID-beige male mice (Charles River). Tumors were harvested 27 or 33 days post-injection, fixed with 10% formalin overnight, embedded in paraffin and cut into 5 µm sections and haematoxylin and eosin staining performed. Teratoma assays were performed by Applied Stem Cell, Inc.

Pathogen testing and cell line authentication

Double FLAG-Halo-mCTCF / mRad21-SNAP_f-V5 knock-in mouse ES cell line clone 59 was pathogen tested using the IMPACT II test, which was performed by IDEXX BioResearch. The C59 cell line was negative for all pathogens including Ectromelia, EDIM, LCMV, LDEV, MAV1, MAV2, mCMV, MHV, MNV, MPV, MVM, *Mycoplasma pulmonis*, *Mycoplasma sp.*, Polyoma, PVM, REO3, Sendai, and TMEV. U2OS cell lines were pathogen tested for mycoplasma using a PCR-based assay as described (Young et al., 2010) (wild-type U2OS) and pathogen tested for mycoplasma using an imaging assay (DAPI staining; C32 knock-in cell line). Both were negative for mycoplasma. Both mouse ES cell and human U2OS cells were authenticated by whole-genome sequencing and morphology (U2OS morphology was compared to U2OS cells obtained from ATCC).

Single molecule imaging

All single-molecule imaging experiments (live-cell residence time measurements, live-cell paSMT at 225 Hz, fixed-cell PALM and fixed-cell dSTORM) were conducted on a custom-built Nikon TI

microscope equipped with a 100x/NA 1.49 oil-immersion TIRF objective (Nikon apochromat CFI Apo TIRF 100x Oil), EM-CCD camera (Andor iXon Ultra 897), a perfect focusing system to correct for axial drift and motorized laser illumination (Ti-TIRF, Nikon), which allows an incident angle adjustment to achieve highly inclined and laminated optical sheet illumination (Tokunaga et al., 2008). The incubation chamber maintained a humidified 37°C atmosphere with 5% CO₂ and the objective was similarly heated to 37°C for live-cell experiments. Excitation was achieved using the following laser lines: 561 nm (1 W, Genesis Coherent) for JF549/PA-JF549 and TMR dyes; 633 nm (1 W, Genesis Coherent) for JF646/PA-JF646 dyes; 405 nm (140 mW, OBIS, Coherent) for all photo-activation experiments. The excitation lasers were modulated by an acousto-optic Tunable Filter (AA Opto-Electronic, AOTFnC-VIS-TN) and triggered with the camera TTL exposure output signal. The laser light is coupled into the microscope by an optical fiber and then reflected using a multi-band dichroic (405 nm/488 nm/561 nm/633 nm quad-band, Semrock) and then focused in the back focal plane of the objective. Fluorescence emission light was filtered using a single band-pass filter placed in front of the camera using the following filters: TMR and JF549/PA-JF549: Semrock 593/40 nm bandpass filter; JF646/PA-JF646: Semrock 676/37 nm bandpass filter. The microscope, cameras, and hardware were controlled through the NIS-Elements software (Nikon).

For simultaneous two-color experiments (dSTORM and PALM experiments), a custom-built setup using two cameras (both Andor iXon Ultra 897 EM-CCD) was used. Cameras were synchronized using a National Instruments DAQ board (NI-DAQ PCI-6723). A single-edge dichroic beamsplitter (Di02-R635-25x36, Semrock) was used to separate two ranges of wavelengths of emission fluorescence. A 676/37 nm bandpass filter (FF01-676/37-25, Semrock) was placed in front of the first camera and 593/40 nm bandpass filter (FF01-593/40-25, Semrock) in front of the second camera.

In “slow-tracking” experiments, to measure residence times, long exposure times (300 ms, 500 ms or 800 ms) and low constant illumination laser intensities (to minimize photobleaching) were used. The camera settings were as follows: normal mode; vertical shift speed: 3.3 μ s; ROI: variable. Generally, each experiment lasted 20 min per cell corresponding to 4000 frames with a 300 ms exposure time, 2400 frames with a 500 ms exposure time and 1500 frames with an exposure time of 800 ms. We recorded 20 min movies from ~6 cells per cell line or condition per day as well as 6 H2B-Halo cells for the photobleaching correction on the same day and all data presented is from at least three independent experiments conducted on different days.

In “fast-tracking” stroboscopic paSMT experiments at ~225 Hz, both the main excitation laser (633 nm for PA-JF646 or 561 nm for PA-JF549) and the photo-activation laser (405 nm) were pulsed. Each frame consisted of a 4 ms camera exposure time followed by a ~447 μ s camera “dead” time. The main excitation laser (633 nm) was pulsed for 1 ms starting at the beginning for the 4 ms camera exposure time. The photo-activation laser (405 nm) was pulsed during the ~447 μ s camera “dead” time, to minimize fluorescent background signal. This sequence was verified using an oscilloscope. The camera settings were as follows: frame transfer mode; vertical shift speed: 0.9 μ s; ROI: height 90 pixels, width variable. Each cell was imaged for 20,000 frames corresponding to ~1.5 min. The photo-activation laser power was optimized to keep an average molecule density of ~0.5 localizations per frame, corresponding to ~10,000 localization per cell per movie. Maintaining a very low density of molecules is necessary to avoid tracking errors. The main excitation laser was used at maximal power. We recorded movies for 8 cells per cell line or condition per day and all data presented is from at least three independent experiments conducted corresponding to at least 24 cells and at least 100,000 localizations.

In PALM experiments, continuous illumination was used for both the main excitation laser (633 nm for PA-JF646 or 561 nm for PA-JF549) and the photo-activation laser (405 nm). However, the intensity of the 405 nm laser was gradually increased over the course of the illumination sequence to image all molecules and at the same time avoid too many molecules being activated at any given frame. The following camera settings were used: 25 ms exposure time; frame transfer mode; vertical shift

speed: 0.9 μ s; ROI: variable. In total, 40,000-60,000 frames were recorded for each cell (~20-25 min), which was sufficient to image and bleach all labeled molecules. After overnight growth on 25 mm plasma-cleaned coverslips and dye labeling and washings, cells were fixed in 4% PFA in PBS for 20 min at 37°C, washed with PBS and then imaged in PBS with 0.01% (w/v) NaN₃ on the same day. All PALM images were acquired at room temperature. All analysis presented contains data from at least 20 cells imaged in at least three independent experiments conducted on different days.

For two-color dSTORM experiments, cell preparation was similar to PALM. After overnight growth on 25 mm plasma-cleaned coverslips and dye labeling and washings, cells were fixed in 4% PFA in PBS for 20 min at 37°C and washed with PBS. We then added 100 nm fluorescent Tetraspeck beads (diluted 1:1000 in PBS; T7279 ThermoFisher Scientific), allowed the beads to settle and washed 3 times with PBS. The coverslips were then stored in PBS with 0.01% (w/v) NaN₃ until imaged later on the same day. C59 Halo-mCTCF / mRad21-SNAP_f mouse ES cells were labeled with 500 nM Halo-JF646 and 500 nM cp-JF549. mES cells stably expressing H2B-SNAP_f were transfected with a plasmid encoding Halo (only; without being fused to anything) and a GFP-NLS protein used for nuclear demarcation. These cells were similarly labeled. Just before imaging, a STORM imaging buffer (very similar to (Boettiger et al., 2016)) was made by mixing 400 μ L 50 mM NaCl, 200 mM Tris pH 7.9 with 150 μ L 50% glucose solution (w/v), 15 μ L GLOX solution, 7.5 μ L COT solution and 50 μ L MEA solution. The GLOX solution was made by mixing 100 μ L 50 mM NaCl, 200 mM Tris pH 7.9 with 7 mg Glucose Oxidase (Sigma-Aldrich) and 25 μ L catalase (16 mg/mL). This solution was made the day before imaging. COT solution was made by dissolving 20.8 mg of Cyclooctatetraene (Sigma-Aldrich 138924-1g) in 1 mL DMSO. COT solution aliquots were stored at -20°C and a fresh aliquot used each time. MEA solution was made by dissolving 77 mg cysteamine (Sigma-Aldrich) in 1 mL water. A few drops of 1 N HCl were added to dissolve the cysteamine. STORM imaging buffer was added to the coverslip with fixed cells, the imaging chamber sealed with parafilm and then immediately loaded on the microscope. Both JF549 and JF646 could be converted into a rapidly blinking state in STORM buffer upon high-intensity laser illumination. For each cell, we exposed cells to high-power 405 nm, 561 nm and 633 nm excitation for ~5-10 seconds. We then acquired 50,000 frames of simultaneous two-color images with constant low intensity 405 nm excitation and high-intensity 561 nm and 633 nm excitation using 25 ms exposure time on both EM-CCD cameras (Andor iXon Ultra 897). Before imaging, we aligned the two cameras using fluorescent beads (100 nm TetraSpeck beads; T7279 ThermoFisher Scientific) to a registration offset below 50 nm. Before imaging each cell, we imaged a cell-adjacent bead. Similarly, after imaging each cell we also imaged a different cell-adjacent bead (1,000 frames at 25 ms each time). We then used the mean offset from the bead measurements before and after imaging a cell for two-color registration for that cell. We estimate a chromatic shift registration error of ~10 nm. The pair cross correlation data presented is from around ~12-18 cells measured on three different days. All PALM and dSTORM experiments on fixed cells were conducted at room temperature to minimize drift.

Analysis of single molecule images

All single-molecule imaging data was processed using a custom-written MATLAB implementation of the MTT algorithm (Sergé et al., 2008). A GUI of this implementation, SLIMfast (Normanno et al., 2015), is available at <https://elifesciences.org/content/5/e22280/supp-material1> (Teves et al., 2016). Briefly, single molecules are localized using bi-dimensional Gaussian fitting (approximating the microscope PSF) subject to a generalized log-likelihood ratio test with a “localization error” threshold (in the range of 10⁻⁶-10⁻⁷), with the option of allowing deflation to detect molecules partially obscured by others. Tracking, that is connecting localizations between consecutive frames, was limited by setting a maximal expected diffusion constant, and takes the trajectory history into account as well as allowing for gaps due to blinking or missed localizations.

For analysis of “slow-tracking” experiments, to measure residence times, the following algorithm parameters were used: Localization error: 10^{-7} ; deflation loops: 1; Blinking (frames): 2; maximum number of competitors: 1; maximal expected diffusion constant ($\mu\text{m}^2/\text{s}$): 0.1.

For analysis of “fast-tracking” stroboscopic paSMT experiments at ~ 225 Hz the following algorithm parameters were used: Localization error: $10^{-6.25}$; deflation loops: 0; Blinking (frames): 1; maximum number of competitors: 3; maximal expected diffusion constant ($\mu\text{m}^2/\text{s}$): 20.

For analysis of PALM experiments the following algorithm parameters were used: Localization error: 10^{-6} ; deflation loops: 0; Blinking (frames): 1; maximum number of competitors: 3; maximal expected diffusion constant ($\mu\text{m}^2/\text{s}$): 0.05.

For analysis of dSTORM experiments we used the same algorithm parameters as for PALM analysis for both color channels.

All subsequent analysis of trajectories was performed using custom-written code in MATLAB as described in detail in the following sections.

Kinetic modeling of fast 225 Hz SMT data

To extract kinetic information from fast stroboscopic paSMT at approximately 225 Hz, we developed and fit a mathematical model to the jump length or displacement distributions. Our approach is largely inspired by an elegant modeling approach previously introduced by Mazza *et al.* (Mazza et al., 2012), but with a number of significant differences and modifications that we will highlight below.

The evolution over time of a concentration of particles located at the origin as a Dirac delta function and which follows free diffusion in two dimensions with a diffusion constant D can be described by a propagator (also known as Green’s function). Properly normalized, the probability of a particle starting at the origin ending up at a location $r = (x, y)$ after a time delay, $\Delta\tau$, is then given by:

$$P(r, \Delta\tau) = N \frac{r}{2D\Delta\tau} e^{-\frac{r^2}{4D\Delta\tau}}$$

Here N is a normalization constant with units of length. In practice, we compare this distribution to binned data. Thus, in practice we integrate this distribution over a small histogram bin window, Δr , to obtain a normalized distribution to compare to the empirically measured distribution. For simplicity, we therefore leave out this normalization constant of subsequent expressions.

Furthermore, in practice we are unable to determine the precise localization of a single molecule. Instead it is associated with a certain localization error, σ , which under our stroboscopic paSMT conditions is approximately 35 nm. Correcting for localization errors is important because it will otherwise appear as if molecules move further between frames than they actually did. Thus, we obtain the following expression for the jump length distribution taking localization error, σ , into account (Matsuoka et al., 2009):

$$P(r, \Delta\tau) = \frac{r}{2(D\Delta\tau + \sigma^2)} e^{-\frac{r^2}{4(D\Delta\tau + \sigma^2)}}$$

DNA binding molecules such as CTCF can generally exist in either a bound or a freely diffusing state. The bound state exhibits very short jump lengths (presumably due to slow chromatin diffusion) and has an associated diffusion constant, D_{BOUND} , whereas the freely diffusing population tends to exhibit much longer jump lengths and has its own associated diffusion constant, D_{FREE} . Next, we assume that binding to chromatin and unbinding from chromatin are both first-order processes with rate constants k_{ON}^* and k_{OFF} . We denote k_{ON}^* with a “*” because it is really a pseudo first-order process since it depends on the concentration of free binding sites: $k_{\text{ON}}^* = [BS_{\text{FREE}}]k_{\text{ON}}$. Thus, the steady-state jump length distribution of a population of molecules that can exist in either their bound or free state is then given by:

$$P(r, \Delta\tau) = F_{\text{BOUND}} \frac{r}{2(D_{\text{BOUND}}\Delta\tau + \sigma^2)} e^{-\frac{r^2}{4(D_{\text{BOUND}}\Delta\tau + \sigma^2)}} + (1 - F_{\text{BOUND}}) \frac{r}{2(D_{\text{FREE}}\Delta\tau + \sigma^2)} e^{-\frac{r^2}{4(D_{\text{FREE}}\Delta\tau + \sigma^2)}}$$

Where F_{BOUND} is the fraction of the population that is bound to chromatin and, $F_{\text{FREE}} = 1 - F_{\text{BOUND}}$, is the fraction of the population that is exhibiting free 3D diffusion. These fractions are related to the first-order rate constants:

$$F_{\text{BOUND}} = \frac{k_{\text{ON}}^*}{k_{\text{ON}}^* + k_{\text{OFF}}} \\ F_{\text{FREE}} = (1 - F_{\text{BOUND}}) = \frac{k_{\text{OFF}}}{k_{\text{ON}}^* + k_{\text{OFF}}}$$

These expressions assume that molecules do not change between their bound and free states during the time delay between frames, $\Delta\tau$. Previous studies have derived analytical expressions to account for this (Mazza et al., 2012; Yeung et al., 2007). However, implementing these expressions numerically greatly slows down fitting the model to the raw jump length distributions. Accounting for state-changes between the free and bound states was necessary in the previous study by Mazza *et al.* (Mazza et al., 2012) because relatively long exposure times (40 ms or 25 Hz) and lag times, $\Delta\tau$, (up to 800 ms) were considered. In this study, we are imaging at a much higher frame-rate (4.4477 ms exposure or ~ 225 Hz) and only consider much shorter lag times, $\Delta\tau$, (up to 7 jumps, i.e. 31.5 ms). Thus, in our case the probability of observing a state-change is much lower. Moreover, the residence time of CTCF (~ 60 -75 s) is much longer than the residence time of p53 (~ 1.8 s) (Mazza et al., 2012). Thus, we can calculate the probability that a bound CTCF molecule unbinds during the longest lag times considered ($\Delta\tau = 31.5$ ms) as:

$$P_{\text{SWITCH}} = 1 - e^{-k_{\text{OFF}}\Delta\tau} \approx 7 \cdot 10^{-5}$$

Thus, accounting for state changes during the lag time, $\Delta\tau$, makes a negligible difference for CTCF. Even if we consider short-lived non-specific interactions, the probability of a state-change is still negligible with our short lag times.

Single-molecule tracking (SMT) is heavily biased towards bound molecules and against freely diffusing molecules for two major reasons. First, almost all single-molecule localization algorithms, including the MTT-algorithm (Sergé et al., 2008) used here, achieve sub-diffraction limit resolution (super-resolution) by treating individual fluorophores as point-source emitters, which generate blurred images that are described by the Point-Spread Function (PSF) of the microscope. 2-dimensional Gaussian modeling of the PSF allows extraction of the particle centroid with sub-pixel resolution. In SMT experiments, this works well for bound molecules, which exhibit negligible movement during the laser exposure time. However, fast moving molecules will tend to “motion-blur” because they can move several pixels during the long exposure times typically used in SMT experiments. “Motion-blurred” particles will thus spread their photons over multiple pixels in the direction of their movement. Therefore, they tend to be missed by most PSF-fitting localization algorithms, which results in a large bias towards bound molecules and a general bias against fast-moving molecules. This means that the bound fraction will be overestimated. To minimize this bias against fast-moving molecules we use stroboscopic illumination where although we have a time delay of $\Delta\tau = 4.4477$ ms, we only laser-illuminate the sample for 1 ms per frame. For a molecule like CTCF where the freely diffusing population has an apparent $D_{\text{FREE}} \sim 2.5 \mu\text{m}^2/\text{s}$, we can calculate the fraction of the population which moves more than a certain length during the 1 ms laser illumination time. Using our imaging setup

(pixel size: 160 nm) less than $\sim 0.0036\%$ (~ 3.6 molecules per 100,000 molecules) of the free CTCF population move more than 2 pixels during the 1 ms laser exposure time. Thus, while we cannot eliminate all bias against moving molecules, our fast stroboscopic SMT methods greatly reduce bias against fast-moving molecules compared to previous approaches.

Second, fast-moving molecules are likely to move out of the focal plane or axial detection window (Δz) during 2D image acquisition. Even though we consider short lag times $\Delta \tau \sim 4.5\text{--}31.5$ ms, this is still long enough for a large fraction of the free population to be lost. As a consequence, bound molecules tend to have much longer trajectories than do free molecules. Again, this means that we are oversampling the bound population and undersampling the free population. To correct for this, we consider the probability that a freely diffusing molecule with diffusion constant, D_{FREE} , will move out of the axial detection window, Δz , during a lag time, $\Delta \tau$. This problem has also been previously considered by Kues and Kubitscheck (Kues and Kubitscheck, 2002). If we consider the extreme case of a population of molecules equally distributed one-dimensionally along an axis, z , with an absorbing boundary at $z_{\text{MAX}} = \Delta z/2$ and $z_{\text{MIN}} = -\Delta z/2$, the fraction of molecules remaining at lag time, $\Delta \tau$, is given by:

$$P_{\text{LEFT}}(\Delta \tau) = \frac{1}{\Delta z} \int_{-\Delta z/2}^{\Delta z/2} \left\{ 1 - \sum_{n=0}^{\infty} (-1)^n \left[\text{erfc} \left(\frac{\frac{(2n+1)\Delta z}{2} - z}{\sqrt{4D_{\text{FREE}}\Delta \tau}} \right) + \text{erfc} \left(\frac{\frac{(2n+1)\Delta z}{2} + z}{\sqrt{4D_{\text{FREE}}\Delta \tau}} \right) \right] \right\} dz \text{ (eqn *)}$$

However, this expression significantly overestimates how many bound molecules are lost since it assumes absorbing boundaries – any molecules that comes into contact with the boundary at $\pm \Delta z/2$ are permanently lost. In reality, there is a significant probability that a molecule, which has briefly contacted or exceeded the boundary, re-enters the axial detection window, Δz , during a lag time, $\Delta \tau$. Moreover, since we allow trajectory gaps of 1 during in our tracking algorithm (i.e. a molecule present in frame n and $n+2$ can still be tracked even if it was not localized in frame $n+1$), we must consider the probability that a lost molecule re-enters the axial detection window during twice the lag time, $2 \Delta \tau$. This results in the somewhat counter-intuitive effect, which was also noted by Kues and Kubitscheck, that the decay rate depends on the microscope frame rate – in other words, the fraction lost depends on how often one “looks”. One approach (Mazza et al., 2012) of accounting for this is to use a corrected axial detection window larger than the true axial detection window: $\Delta z_{\text{CORR}} > \Delta z$.

To find the corrected axial detection window, we first measured the true empirical axial detection window, Δz . We labeled C59 Halo-mCTCF mouse embryonic stem cells and C32 Halo-hCTCF human U2OS cells grown on plasma-cleaned 25 mm #1.5 cover glasses with JF646 at a low enough density to clearly observe single molecules and fixed them in 4% PFA in PBS for 20 min. We then collected an extensive z -stack throughout the nucleus with a range of 6 μm and a step size of 20 nm (301 frames) and imaged single molecules at a signal-to-background ratio comparable to the one used during our fast 225 Hz paSMT experiments. We tracked molecules using the MTT algorithm (Sergé et al., 2008) and the same parameters used for our paSMT experiments. We then analyzed the survival curve, corrected for photobleaching, of single JF646-labeled Halo-CTCF molecules as a function of the step size and found the axial detection window to be approximately $\Delta z \approx 700$ nm and highly similar in U2OS and mES cells under HiLo-illumination (Tokunaga et al., 2008).

Next, we performed Monte Carlo simulations following the Euler-Maruyama scheme. For a given diffusion constant, D , we randomly distributed 50,000 molecules one-dimensionally along the z -axis from $z_{\text{MIN}} = -\Delta z/2 = -350$ nm to $z_{\text{MAX}} = \Delta z/2 = 350$ nm, where $\Delta z \approx 700$ nm. Next, using a time-step of $\Delta \tau = 4.4477$ ms, we simulated one-dimensional Brownian diffusion along the z -axis by randomly picking Gaussian-distributed numbers from a normal distribution with parameters: $\mu = 0$; $\sigma = \sqrt{2D\Delta \tau}$ using the function `normrnd` in MATLAB. For time gaps from 1 $\Delta \tau$ to 15 $\Delta \tau$ we then calculated the fraction of molecules that were lost, allowing for one missing frame as in our tracking algorithm. We repeated these simulations for particles with diffusion constants in the range of $D=1 \mu\text{m}^2/\text{s}$ to $D=12$

$\mu\text{m}^2/\text{s}$ to generate a comprehensive dataset over a range of biologically plausible diffusion constants. We then performed least-squares fitting of this dataset to equation * using a corrected Δz_{CORR} :

$$\Delta z_{\text{CORR}} = \Delta z + a\sqrt{D} + b$$

The simulated data were well fit using this corrected axial detection window and we found the following best-fit parameters: $a = 0.15716 \text{ s}^{-1/2}$; $b = 0.20811 \mu\text{m}$. Practically, we evaluated equation * using numerical integration in MATLAB and aborted the infinite sum once the absolute value of another iteration fell below 10^{-12} . We performed non-linear least-squares fitting in MATLAB by stochastically generating random parameter guesses for a and b as a starting point for the least-squares fitting routine `lsqcurvefit` and iterating using multiple random input guesses to avoid local minima.

Having derived an analytical expression for the probability of a free molecule being lost due to axial diffusion during the imaging time, we can now thus write down the final equations using for fitting the raw jump length distributions:

$$P(r, \Delta\tau) = F_{\text{BOUND}} \frac{r}{2(D_{\text{BOUND}}\Delta\tau + \sigma^2)} e^{-\frac{r^2}{4(D_{\text{BOUND}}\Delta\tau + \sigma^2)}} + Z_{\text{CORR}}(\Delta\tau)(1 - F_{\text{BOUND}}) \frac{r\Delta r}{2(D_{\text{FREE}}\Delta\tau + \sigma^2)} e^{-\frac{r^2}{4(D_{\text{FREE}}\Delta\tau + \sigma^2)}}$$

where:

$$Z_{\text{CORR}}(\Delta\tau) = \frac{1}{\Delta z} \int_{-\Delta z/2}^{\Delta z/2} \left\{ 1 - \sum_{n=0}^{\infty} (-1)^n \left[\text{erfc}\left(\frac{(2n+1)\Delta z}{2} - z\right) + \text{erfc}\left(\frac{(2n+1)\Delta z}{2} + z\right) \right] \right\} dz$$

and:

$$\Delta z = 0.700 \mu\text{m} + 0.15716 \text{s}^{-1/2} \sqrt{D} + 0.20811 \mu\text{m}$$

In practical terms, we consider the jump length or displacement distributions for timepoints 1 to 8, corresponding to 7 jumps with delays from $1\Delta\tau$ to $7\Delta\tau$ (i.e. this includes 6 jumps of $1\Delta\tau$, 5 jumps of $2\Delta\tau$, and so on). Thus, the probability of seeing a free molecule present in the first frame is higher in the second frame than in the seventh frame according to the Z_{CORR} equation above. While we have many trajectories that are much longer than 8 localizations, we refrain from using the entire trajectories since almost all very long trajectories (e.g. > 100 localizations) are highly biased towards bound molecules. While the above Z_{CORR} equation should in principle correct for this, at long time lags the probability of still seeing a moving molecule approaches zero and thus small errors in the Z_{CORR} equation, which is an approximation, is likely to strongly affect the estimation of the bound fraction.

We note that a question arises of whether to use the entire trajectory or not. One bias against moving molecules is that frequently, freely diffusing molecules will translocate through the axial detection window, Δz , yielding only a single detectable localization and thus no jumps to be counted. Conversely, one bias against bound molecules, is that moving molecules can re-enter the axial detection window multiple times resulting in the same molecule appearing as multiple distinct trajectories and thus being over-counted. Clearly, the extent of the bias will depend on the photobleaching rate – in the limit of no photobleaching, a single freely diffusing molecule could yield a very high number of different trajectories, leading to large over-counting of the free population. However, in practice, under our stroboscopic paSMT conditions, the average dye lifetime is quite short. We note that dye disappearance is both due to photoblinking and blinking, but note that blinking should not affect estimates of the fraction bound. The actual mean number of frames depends on the fraction bound and diffusion constant – proteins with slow diffusion constants and a high bound fraction stay in the axial detection volume for longer and thus yield longer trajectories. For Halo-mCTCF, the mean number of frames per trajectory is ~ 3 -4, whereas for Halo-3xNLS it is less than 2. We took two approaches to test whether the fraction of the trajectory that is included in the modeling would strongly affect the fraction bound estimate: analysis of our raw data and Monte Carlo simulations according to the Euler-

Maruyama scheme. First, in the case of our raw data, the difference between using only the first 7 jumps and using the entire trajectory only affects the fraction bound estimate by a few percentage points, suggesting that it makes a minor difference under conditions where photobleaching and blinking results in relatively short trajectories. Second, we performed Monte Carlo simulations following the Euler-Maruyama scheme and with the following assumptions: 50% of molecules are bound and the free diffusion constant is $2.5 \mu\text{m}^2/\text{s}$; the axial detection volume is 700 nm and the laser excitation beam under highly inclined and laminated optical sheet illumination (HiLo) illuminates $\sim 4 \mu\text{m}$ (Tokunaga et al., 2008), corresponding to half the nucleus (nuclear diameter: $8 \mu\text{m}$); molecules within the HiLo sheet photobleach with a constant rate (thus molecules can photobleach outside of the detection slice as in our experiments); the 2D localization error is 35 nm and the timestep is 4.5 ms; since the vast majority of trajectories lasts no more than tens of milliseconds, but both the CTCF unbinding rate ($\sim 1 \text{ min}$) and re-binding rate ($\sim 1 \text{ min}$) are much slower, we ignore changes in state (bound vs. free) during the trajectory lifetime; Brownian motion was simulated for 500,000 trajectories in 3 dimensions enclosed within the nucleus by picking random numbers in each dimension from a normal distribution defined as: $N \sim (0, \sqrt{2D\Delta\tau})$. Our simulations showed that our paSMT modeling approach could accurately infer both the free diffusion constant (slight overestimate of D , but error less than 5%) and the fraction bound and that using the entire trajectory leads to a very small overestimate of the bound fraction (1 percentage point) and that using the first 7 jumps only leads a small underestimate of the bound fraction (~ 3 percentage points) under conditions where the mean trajectory length (~ 3) was similar to the mean trajectory length for Halo-mCTCF in mESCs under our experimental conditions. However, under conditions with negligible photobleaching and extremely long trajectories of a mean length of ~ 100 frames, using only the first 7 jumps leads to a serious underestimate of the bound fraction. We note that it is not experimentally realistic to obtain trajectories of this length with currently available dyes and microscope modalities and thus not relevant in this case, but we nevertheless note that generalizing the approach to trajectories of any length is an interesting future direction. Finally, because of the numerous other biases against free molecules noted above, we only use the first 7 jumps and ignore all subsequent jumps in longer trajectories for our model fitting in this case.

We then fit the above equation for, $P(r, \Delta\tau)$, to the raw jump lengths distributions for time gaps of $1 \Delta\tau$ to $7 \Delta\tau$ corresponding to 4.5 ms to 31.5 ms. Although we show the fit function to the probability density, i.e. histograms (Figure 3A-E), this introduces binning artifacts (bin: 10 nm). Thus, we instead fit the model to the cumulative distribution function (CDF) calculated from the data. The model has three fit parameters, D_{BOUND} , D_{FREE} and F_{BOUND} , and is fit to the combined jump length CDFs (from $1 \Delta\tau$ to $7 \Delta\tau$) using least squares fitting. We constrain D_{BOUND} to a range of $[0.0005; 0.08] \mu\text{m}^2/\text{s}$, but note that slight errors in the estimation of the localization error would make it appear as if the bound molecules move faster than they actually do. F_{BOUND} is of course constrained to a range of $[0; 1]$ and we only constrain D_{FREE} to be greater than $0.15 \mu\text{m}^2/\text{s}$. We randomly generated initial parameter guesses for D_{BOUND} , D_{FREE} and F_{BOUND} and then fit the model to the seven CDFs through non-linear least squares minimization implemented in MATLAB through the function `lsqcurvefit`. We then repeat this for multiple iterations of random initial parameter guesses and record the best-fit parameters. Thus, from the kinetic modeling we obtain D_{BOUND} , D_{FREE} and F_{BOUND} , from which we can also calculate $F_{\text{FREE}} = 1 - F_{\text{BOUND}}$. We note that though the previous study on p53 by Mazza *et al.* (Mazza et al., 2012) required two freely diffusive states and one bound state to fit the jump length distributions, in our case a single free diffusion state and one bound state was sufficient to accurately fit the raw jump length distributions. Thus, we did not consider the possibility of additional diffusive states.

Inferring parameters related to the CTCF and Rad21 target search mechanism

Next, we sought to further extend our knowledge of the nuclear target search mechanism *in vivo* using the parameters inferred from our kinetic modeling of the fast paSMT data as well as our residence

time measurements. First, we illustrate the approach using CTCF as an example. We will continue with the steady-state 2-state model (bound or free) introduced above, but further distinguish specific and non-specific binding. From the kinetic model fitting above we determine the total bound fractions for CTCF to be: mESC C59 Halo-mCTCF, $68.0\% \pm 3.3\%$; mESC C87 Halo-mCTCF, $68.4\% \pm 2.1\%$; U2OS C32 Halo-hCTCF, $58.9\% \pm 2.0\%$. However, this total bound fraction contains both CTCF molecules bound specifically to their cognate binding sites and non-specific interactions. For example, sliding on DNA would be indistinguishable from stable binding to a cognate site under our paSMT conditions (localization error ~ 35 nm). We estimate the fraction that is non-specifically bound using a mutant CTCF, 11ZF-mut-Halo-mCTCF, where we have introduced mutations into the DNA binding domain. This mutant contains a His-to-Arg mutation in each of the 11 zinc-finger domains. Since the mutant, by design, is unable to interact specifically with chromatin through its zinc-finger domains, we reason that this mutant interacts only non-specifically. From our kinetic model fitting of the 11ZF-mut-Halo-mCTCF jump length histograms we estimate the bound fraction for this mutant to be $19.1\% \pm 4.1\%$ in mouse ES cells and 17.7% in human U2OS cells. Thus, the specifically bound fraction can be calculated according to:

$$F_{\text{BOUND, specific}} = F_{\text{BOUND, total}} - F_{\text{BOUND, non-specific}}$$

Using the numbers above, we then obtain the following estimates for the specifically bound fraction: mESC C59 Halo-mCTCF, 48.9% ; mESC C87 Halo-mCTCF, 49.3% ; U2OS C32 Halo-hCTCF, 41.2% . We note that this estimation is associated with definitional uncertainty as well measurement uncertainty. It is difficult to define exactly what a non-specific interaction is, but it likely involves transient binding and/or sliding on DNA. It is also difficult to define precisely for how long a molecule has to associate with DNA for that to be reasonably counted as a non-specific interaction. Nevertheless, if we operationally define non-specific interaction here as an interaction present after mutation of the DNA binding domain, we can proceed with investigating the target search mechanism.

Next, we would like to determine the average time it takes a single CTCF protein to find another specific binding site. In the following, we will use “s” and “ns”, as abbreviations for specific and non-specific, respectively. The pseudo-first-order rate constant for specific binding sites, $k_{\text{ON,s}}^*$, is related to the fraction bound by:

$$F_{\text{BOUND,s}} = \frac{k_{\text{ON,s}}^*}{k_{\text{ON,s}}^* + k_{\text{OFF,s}}} \Leftrightarrow k_{\text{ON,s}}^* = \frac{F_{\text{BOUND,s}} k_{\text{OFF,s}}}{1 - F_{\text{BOUND,s}}}$$

We determined the off-rate for a specific interaction in our residence time measurements (Figure 2). Thus, from the previously determined values of $F_{\text{BOUND,s}}$ and $k_{\text{OFF,s}}$, we can calculate $k_{\text{ON,s}}^*$. $k_{\text{ON,s}}^*$ is an interesting constant because it is directly related to the average search time for a specific CTCF binding site:

$$\tau_{\text{search,s}} = \frac{1}{k_{\text{ON,s}}^*} = \frac{1 - F_{\text{BOUND,s}}}{F_{\text{BOUND,s}} k_{\text{OFF,s}}}$$

When we plug in the previously determined values of $F_{\text{BOUND,s}}$ and $k_{\text{OFF,s}}$, we thus obtain total search times of: mESC C59 Halo-mCTCF, ~ 65.9 s; mESC C87 Halo-mCTCF, ~ 62.6 s; U2OS C32 Halo-hCTCF, ~ 102.8 s. We note that the search times depend sensitively on $k_{\text{OFF,s}}$, such that if a CTCF residence time of ~ 4 min is used instead, the search time also increases to around 4 min in mES cells and to ~ 5.7 min in U2OS cells. Regardless of the total search time, CTCF molecules spend roughly 50% of their time searching for binding sites in mES cells and roughly 60% of their time searching for binding sites in human U2OS cells. This search time contains intermittent periods of free 3D diffusion interrupted by brief non-specific binding or sliding interactions on chromatin. E.g. for mESC C59 Halo-mCTCF, 51.1% of the total time is spent searching - 19.1% of the total time is spent in 1D sliding on DNA or transient interactions and 32.0% of the total time is spent on free 3D diffusion. Since we know the average search time to be ~ 65.9 s, we can thus calculate that during this average search time, ~ 41.3 s are spent in free 3D diffusion and ~ 24.6 s are spent in non-specific DNA

interactions such as sliding. Thus, for mESC C59 Halo-mCTCF roughly 37% of the total search time is spent in non-specific DNA interactions and roughly 63% of the time is spent on free 3D diffusion. Similar analysis of C32 Halo-hCTCF in human cells show that 58.8% of the total time is spent searching, with 17.7% of the total time in non-specific chromatin association (e.g. 1D sliding) and 41.1% of the total time in free 3D diffusion. Thus, with an average search time of ~ 102.8 s, human Halo-hCTCF spends on average ~ 30.9 s on non-specific chromatin association and ~ 71.9 s on free 3D diffusion.

We can apply the same approach to cohesin as measured by following mRad21 in mES cells. We note that the above approach assumes a single bound state and a single free state. This is certainly too simplistic in S/G2, since our FRAP experiments suggest that the chromatin residence time of cohesin involved in sister chromatid cohesion is likely much longer than the cohesin involved in chromatin looping. Moreover, it is far from clear that the ON-rate, i.e. topological loading of cohesin onto chromatin, would be similar for cohesin involved in chromatin looping and in sister chromatid cohesion. Thus, we restrict our analysis to G1. Even then, we stress that this analysis assumes that all topologically engaged G1 cohesin has the same ON- and OFF-rates. We estimated the G1 cohesin residence time to be 19.51 min (C45 mRad21-Halo) and 24.16 min (C59 mRad21-SNAP). In the following, we will use the mean: 21.8 min. Using stroboscopic paSMT we estimated the G1 total fraction bound of cohesin to be $53.5\% \pm 4.1\%$ and the non-specifically bound fraction to be $13.7\% \pm 3.1\%$ using a mutant (F601R, L605R, Q617K) that is reported to be unable to form cohesin complexes (Haering et al., 2004). Thus, 39.8% of cohesin is topologically bound to chromatin, 13.7% non-specifically associated with chromatin and 46.5% in free 3D diffusion in G1-phase of the cell cycle. Non-specific chromatin association may include non-productive topological loading attempts. This yields a search time of ~ 33.0 min of which around 7.51 min is spent on non-specific chromatin association (e.g. sliding) and 25.49 min is spent on free 3D diffusion. We note that this description of the cohesin search mechanism is somewhat simplified since assisted topological loading is a bit more complicated than finding a cognate binding site for a typical sequence-specific transcription factor. Rather, it is likely that the cohesin search mechanism is regulated by other protein interaction partners and by post-translational modifications (Skibbens, 2016). Nevertheless, even if topological loading involves multiple steps, the process can be described as a single first-order reaction if there is a single rate-limiting step.

Residence time measurements from SMT

To extract residence times from SMT data recoded at long exposure time, we took a hybrid approach related to that of (Chen et al., 2014) and (Mazza et al., 2012). Briefly, we took advantage of long exposure times (300 ms, 500 ms or 800 ms) as previously described (Chen et al., 2014): this causes freely-diffusing molecules to motion-blur into the background such that they are generally missed by our detection algorithm (Sergé et al., 2008). We then recorded the trajectory length of each “bound” molecule and used these to generate a survival curve (1-CDF). However, as previously reported there are multiple contributions to this survival curve beyond specific binding, which is what we are interested in, such as non-specific binding (Chen et al., 2014) and slow-diffusing molecules (Mazza et al., 2012). Beyond these two, localization errors can cause both false positive and false negative detections. False negative detections especially occur for molecules close to being out-of-focus. This can cause a single long trajectory to appear as many short ones. Thus, we performed double-exponential fitting (corresponding to specific and non-specific binding) using:

$$P(t) = Ae^{-k_{ns}t} + Be^{-k_s t}$$

where k_{ns} corresponds to the unbinding rate for non-specific binding and k_s corresponds to the unbinding rate constant for specific binding. We note that the first rate constant, k_{ns} , is likely to be contaminated by localization errors (e.g. from molecules close to being out-of-focus) and experimental noise and we therefore caution against over interpreting it. To filter out contributions from tracking

errors and slow-diffusing molecules, we applied an objective threshold as previously described to consider only particles tracked for at least N_{\min} frames (Mazza et al., 2012). To determine N_{\min} , we plotted the inferred residence time as a function of N_{\min} and observed convergence to a single value after ~ 2.5 s (i.e. 8 frames at 300 ms exposure time, 5 frames at 500 ms exposure time, 3 frames at 800 ms exposure time; Figure 2–Figure Supplement 1A). We thus used this threshold to determine the value of k_s . The measured k_s , however, reflects both unbinding from chromatin as well as photobleaching etc.:

$$k_s = k_{s,\text{true}} + k_{\text{bias}}$$

Photobleaching clearly needs to be corrected for. But several other factors also contributed faster apparent unbinding. Among these were axial cell drift, lateral cell drift, fluctuating background and others. Axial cell drift can cause a single molecule to move gradually out-of-focus, which appears as unbinding. We also observe significant lateral cell drift, especially for mES cells due to cell movement, which can appear as unbinding if particle movement exceeds the threshold. Drift is especially an issue for molecules exhibiting relatively stable binding such as CTCF, where we occasionally, but very rarely, observe single molecules for around 10 min under constant laser illumination. To correct for all of these factors including photobleaching, we reasoned that, if we assume that all of these processes are Poisson processes, then the sum of independent Poissons is also a Poisson. If we further assume that these processes will affect H2B-Halo to the same extent as CTCF (i.e. photobleaching depends only on the dye used and the laser intensity; axial chromatin or cell drift is the same for Halo-CTCF cells as for H2B-Halo cells), then we can measure an apparent unbinding rate for H2B-Halo and use this as k_{bias} . This analysis assumes that any apparent unbinding of H2B will be due to photobleaching or drift etc., which is consistent with our FRAP data. However, we note that although H2B molecules are no doubt occasionally evicted from chromatin (e.g. during chromatin remodeling), as long as the rate is much smaller than the unbinding rate of CTCF, this makes a negligible contribution. Thus, to estimate k_{bias} , we repeated the experiments on mES or U2OS cells stably expressing H2B-Halo and estimated k_{bias} as the slow component from double-exponential fitting as described above. We always performed the H2B-Halo control experiment on the same day as the other experiments. Having measured k_{bias} , we then calculated the residence time as

$$\tau_s = \frac{1}{k_{s,\text{true}}}$$

We note that the above analysis assumes that the unbinding rate for all CTCF sites is identical, which is clearly an approximation, though the ability of the model to fit the data suggests it is a reasonable approximation. However, this analysis would miss a very small CTCF fraction ($<3\%$) showing different residence times. So the above calculated residence time should be interpreted as an average residence time, which holds for most CTCF sites, but may not hold for all.

PALM – data processing and clustering analysis

We extracted single-molecule x,y coordinates from single-color PALM images using the following pipeline. We took advantage of the high photostability of the PA-JF549 and PA-JF646 dyes to increase localization accuracy and to perform drift correction. Similar fiducial marker independent drift-correction algorithms have been described previously (Elmokadem and Yu, 2015; Wang et al., 2014). At the laser intensity used and an exposure time of 25 ms, each JF549/JF646 molecule lasted ~ 5 -10 frames on average before photobleaching. Thus, after localizing molecules in each frame and tracking them between frames, we obtaining several estimates of the true x,y coordinates for each molecule, which improves the localization precision. Moreover, since each frame contained 5-10 molecules on average this allowed us to perform drift correction by tracking the average drift of particles over time after binning to average out noise in individual localizations.

For spatial clustering analysis, we segmented the nucleus by convolving the PSF with the single-molecule localizations and then blurring the image using iterative Gaussian smoothing followed by

thresholding or by manual polygon segmentation. We then divided the nucleus into partially overlapping 3 μm squares and performed clustering analysis on these squares using a recently reported Bayesian algorithm (Rubin-Delanchy et al., 2015). We used the same prior as published (Rubin-Delanchy et al., 2015) and performed cluster identification and characterized clusters according to their cluster radius and fraction of molecules in clusters as described (Rubin-Delanchy et al., 2015).

A major concern in clustering analysis of PALM images is photo-blinking, where a dye turns off for some frames and the re-appears. Since we track single molecules across frames and allow for gaps of 1 frame, most molecules that exhibit multiple appearances will be collapsed into a single localization. However, it is not possible to unambiguously distinguish two different co-localizing molecules that appear many frames apart, from a single molecule that exhibits a long photo-blink. Thus, to investigate to what extent the apparent clustering that we observe is due to uncorrected photo-blinking we took the following approaches.

First, we compared our Halo-CTCF and Rad21-Halo PALM reconstructions to H2B-Halo and Halo-3xNLS. While there is no known protein whose nuclear organization perfectly exhibits complete spatial randomness, we reasoned that Halo-3xNLS should exhibit a relatively uniform distribution. Thus, by using the same dye and imaging conditions as for CTCF and Rad21, we treat the level of clustering observed for Halo-3xNLS as being largely due to blinking, and thus generate a “blinking floor”. Since both CTCF and Rad21 exhibits much higher clustering than Halo-3xNLS (Figure 4–Figure Supplement 1C), we conclude that most of the observed clustering is not due to photo-blinking. We note that both the H2B-Halo and Halo-3xNLS transgenes are expressed at very high levels. Thus, we empirically adjusted the PA-JF549 concentration so as to get similar numbers of localizations as for CTCF, so as to exclude any bias coming from the number of molecules.

Second, in mES cells CTCF and H2B exhibit comparable levels of clustering, but Ripley’s $L(r)$ - r curves are qualitatively different, with H2B showing clustering at larger length scales. This further suggests that our PALM approach is measuring real clustering and that the relatively small clusters observed for CTCF and Rad21 are not merely photo-blinking artefacts.

Third, we performed two-color labeling and imaging to unambiguously distinguish true clusters from photo-blinking. We labeled Halo-hCTCF in C32 U2OS cells with approximately equimolar concentrations of PA-JF549 and PA-JF646 dyes and performed 2-color PALM. Since each Halo-Tag can only bind one dye, any cluster composed of N molecules should under ideal circumstances exhibit a binomial distribution of JF549 and JF646 molecules. That is, the probability of a cluster composed of N CTCF molecules having k JF549-conjugated CTCF molecules should follow:

$$P(X_{\text{JF549}} = k) = \binom{N}{k} p_{\text{JF549}}^k (1 - p_{\text{JF549}})^{N-k}$$

where

$$p_{\text{JF549}} = \frac{N_{\text{JF549}}}{N_{\text{JF549}} + N_{\text{JF646}}}$$

is the fraction of all dye-labeled nuclear CTCF molecules that was labeled with JF549. Conversely, consider the other extreme case where all clusters are exclusively due to photo-blinking artifacts. In this extreme scenario, all clusters should be exclusively composed of JF549-conjugated CTCF molecules or exclusively composed of JF646-conjugated CTCF molecules. If we plot the probability density function for the fraction of JF549-labelled molecules in clusters, the idealized case should show a binomial distribution with a peak at p_{JF549} . On the other hand, the extreme “photo-blinking only” case should show a probability density function for the fraction of JF549-labelled molecules in clusters with peaks at 0 and 1 and nothing in between, corresponding to exclusive JF549 and exclusive JF646 clusters. Thus, to apply this analysis we merged all JF549 and JF646 localizations and applied the Bayesian cluster identification algorithm to the merged dataset. We then analyzed all of the called clusters that were composed of at least 10 detections. We consider only these clusters since for very small clusters the probability of finding clusters exclusively in one color is significant even in the ideal binomial case.

In a given nucleus, hundreds of clusters fulfilled this criterion (>10 detections). To robustly compare this to the ideal binomial case, for each cluster of size N we generated binomial random clusters using `binornd` in MATLAB. Finally, we compared the distribution of cluster compositions for the observed clusters and the binomial random clusters in Figure 4–Figure Supplement 1E. Since each nucleus had a slightly different fraction of molecules labeled with JF549 and JF646, we only show the distribution for a single nucleus. As can be seen, the deviation from the binomial case is small. Essentially all clusters at this size contains molecules of both colors demonstrating that clustering is not exclusively a photo-blinking artifact. Thus, although some clustering is clearly due to photo-blinking, the majority of clusters are composed of multiple distinct molecules. To summarize the results for multiple cells, we also calculated the Kullback-Leibler divergence between the expected binomial and observed distributions for each cell. The mean Kullback-Leibler divergence was ~ 0.3 bits further demonstrating that most clusters are not a photo-blinking artifact. Finally, we note that a recent paper demonstrates that PA-JF549 shows limited photo-blinking (Grimm et al., 2016).

Two-color dSTORM – data processing and pair correlation analysis

We processed two-color dSTORM data essentially identically to PALM data. After chromatic registration, blinking-correction and drift-correction using the same approach as for PALM analysis, nuclei were manually segmented using polygon segmentation based on a rough image generated by convolving the PSF with the single-molecule localizations and then blurring the image. We note that SNAP-tag dye-labeling is somewhat less specific than HaloTag labeling (Figure 1–Figure Supplement 1) – in particular, when we label wild-type cells that do not express a SNAP-tag protein with cp-JF549 (or any other SNAP dye) we observe enrichment along the nuclear envelope that does not disappear even after extensive washings. Labeling inside the nucleus, however, appears to be specific with cp-JF549, but less so with SNAP-TMR (compare Figure 1–Figure Supplement 1B and 1C). To avoid this affecting our dSTORM analysis, we segmented out the nuclear envelope during segmentation of the nucleus. Images (such as Figure 4A) were generated by binning single-molecule localizations into square pixel-bins of 10 nm and then false-color rendering JF549 localizations in green and JF646 localizations in magenta, such that saturating co-localization appears white. We note that co-localization of two single molecules are therefore not visible in these rendered images. Only overlap of clusters with saturating brightness appear white. Thus, most co-localizing CTCF and Rad21 molecules are not visible in Figure 4A. Thus, as a much more quantitative analysis we performed pair cross correlation analysis. Like pair correlation analysis, which quantifies the spatial interaction of proteins with themselves (i.e. clustering), pair cross correlation analysis quantifies interactions between two different proteins. Thus, $C(r)$ quantifies enrichment between two different proteins as a function of interparticle distance, r . When the two proteins are independent (Complete Spatial Randomness (CSR)), $C(r) = 1$ for all r . We calculate $C(r)$ using the whole nucleus and edge-correction as previously described (Stone and Veatch, 2015) using bins of 10 nm. The main way in which pair cross correlation can cause false positive pair cross correlation is through fluorophore bleedthrough during simultaneous two-color imaging. E.g. if 561 nm excited J549 molecules emit enough far-red photons to be detected in the JF646 channel, this would result in high, but false positive, pair cross correlation at small r . To rule out bleedthrough and any other bias, we also imaged a mES cell line stably expressing H2B-SNAP_f transfected with a plasmid encoding a free Halo protein. We expect no significant co-localization between these proteins beyond mild exclusion from certain nuclear regions (e.g. nucleolar regions). In agreement, their experimentally observed pair cross correlation was not significantly different from CSR at any r . Since these cells were imaged under the same conditions as C59 Halo-mCTCF/mRad21-SNAP_f, this rules out the possibility that the observed pair cross correlation at small r between CTCF and cohesin is due to fluorophore bleedthrough or any other technical artifact.

Antibodies

Antibodies were as follows: ChromPure rabbit and mouse normal IgG from Jackson ImmunoResearch; anti-CTCF for Western Blot (WB) from Millipore (EMD 07-729), for ChIP and Co-IP from Abcam (ab128873); anti-Rad21 for WB and ChIP from Abcam (ab154769), for CoIP from Millipore (EMD 05-908); anti-SMC1 and anti-SMC3 from Bethyl (A300-055A, A300-060A); anti-FLAG from Sigma-Aldrich (F7425); anti-TBP, anti-H3, and anti-V5 from Abcam (ab51841, ab1791, ab9116).

Chromatin immunoprecipitation (ChIP) and ChIP-seq libraries

ChIP assays in wild-type and double CTCF/Rad21 knock-in (clone C59) mouse JM8N4 mES cells were performed essentially as described (Testa et al., 2005) with minor modifications. Cells were cross-linked for 5 minutes at room temperature with 1% formaldehyde-containing medium; cross-linking was stopped by PBS-glycine (0.125 M final). Cells were washed twice with ice-cold PBS, scraped, centrifuged for 10 min at 4000 rpm, resuspended in cell lysis buffer (5 mM PIPES, pH 8.0, 85 mM KCl, and 0.5% NP-40, 1 ml/15 cm plate) and incubated for 10 min on ice. During the incubation, the lysates were repeatedly pipetted up and down every 5 minutes. Lysates were then centrifuged for 10 min at 4000 rpm. Nuclear pellets were resuspended in 6 volumes of sonication buffer (50 mM Tris-HCl, pH 8.1, 10 mM EDTA, 0.1% SDS), incubated on ice for 10 min, and sonicated to obtain DNA fragments below 2000 bp in length (Covaris S220 sonicator, 20% Duty factor, 200 cycles/burst, 100 peak incident power, 50 cycles of 30" on and 30" off). Sonicated lysates were cleared by centrifugation and 400-1600 μ g of chromatin was diluted in RIPA buffer (10 mM Tris-HCl, pH 8.0, 1 mM EDTA, 0.5 mM EGTA, 1% Triton X-100, 0.1% SDS, 0.1% Na-deoxycholate, 140 mM NaCl) to a final concentration of 0.8 μ g/ μ l, precleared with Protein A sepharose (GE Healthcare) for 2 hours at 4°C and immunoprecipitated overnight with 8-16 μ g of normal rabbit IgGs, anti-Rad21 or anti-CTCF antibodies. About 15% of the precleared chromatin was saved as input. Immunoprecipitated DNA was purified with the Qiagen QIAquick PCR Purification Kit, eluted in 60 μ l of water and analyzed by qPCR together with 2% of the input chromatin prior to ChIP-seq library preparation (SYBR® Select Master Mix for CFX, ThermoFisher, see Supplementary File 2 for primer sequences).

ChIP-seq libraries were prepared independently from two ChIP biological replicates using the Illumina TruSeq™ DNA sample preparation kit according to manufacturer instructions with few modifications. We used 100 ng of ChIP input DNA (as measured by Fragment analyzer™) and 50 μ l of immunoprecipitated DNA as a starting material; Illumina adapters were diluted 1:50, and library samples were enriched through 18 cycles of PCR amplification. We assessed library quality and fragment size by qPCR and Fragment analyzer™, and when necessary we performed an additional size selection step on agarose gel after PCR amplification to enrich for fragments between 150 and 500 bp. We sequenced 4 to 8 multiplexed libraries per lane on the Illumina HiSeq4000 sequencing platform (single end-reads, 50 bp long) at the Vincent J. Coates Genomics Sequencing Laboratory at UC Berkeley, supported by NIH S10 OD018174 Instrumentation Grant.

ChIP-seq analysis

Input, IgG, Rad21 and CTCF ChIP-seq raw reads from wild type and knock-in ESCs from two biological replicates (18 libraries total, see Supplementary File 1) were quality-checked with FastQC and aligned onto the mouse genome (mm10 assembly) using Bowtie (Langmead et al., 2009), allowing for two mismatches (-n 2) and no multiple alignments (-m 1). Enriched regions were visualized on the mm10 genome with the Integrative Genomics Viewer (IGV) (Robinson et al., 2011; Thorvaldsdóttir et al., 2013), after creating tiled data files from alignment files (igvtools count -w 50 -e 200). Peaks were called with MACS2 (--nomodel --extsize 250) (Zhang et al., 2008) combining inputs from the two replicates as a control, first for each biological replicate separately, and then, after having verified that results were highly reproducible, for the merged replicates (Supplementary File 1). Coverage and overlap between ChIP-seq peaks across samples and with previously published CTCF and Rad21

datasets were computed through Galaxy (Blankenberg et al., 2010; Giardine et al., 2005; Goecks et al., 2010), requiring a minimum 1-bp overlap between peak intervals (Supplementary File 1).

To create heatmaps we used deepTools (version 2.4.1) (Ramirez et al., 2016). We first ran bamCoverage (--binSize 50 --normalizeTo1x 2150570000 --extendReads 250 --ignoreDuplicates -of bigwig) and normalized read numbers of WT and C59 IgG, CTCF and Rad21 merged replicates to 1x sequencing depth, obtaining read coverage per 50-bp bins across the whole genome (bigWig files). We then used the bigWig files to compute read numbers across 6 kb centered on either WT CTCF or WT Rad21 peak summits as called by MACS2 (computeMatrix reference-point --referencePoint=TSS --upstream 3000 --downstream 3000 --missingDataAsZero --sortRegions=no). We sorted the output matrices by decreasing WT enrichment, calculated as the total number of reads within a MACS2 called ChIP-seq peak. Finally, heatmaps were created with the plotHeatmap tool (--averageTypeSummaryPlot=mean --colorMap='Blues' --sortRegions=no).

RT-qPCR analysis

Total RNA was purified from cell pellets using RNeasy Plus Mini kit (Qiagen) and quantified by Nanodrop. For RT-qPCR, 1 µg of total RNA was retrotranscribed to cDNA with oligo(dT) primers (Ambion, Life Technologies) and Superscript III (Invitrogen). 2 µl of 1:40 cDNA dilutions were used for quantitative PCR (qPCR) with SYBR® Select Master Mix for CFX (Applied Biosystems) on a BIO-RAD CFX Real-time PCR system (see Supplementary File 2 for primer sequences).

Western Blot and co-immunoprecipitation (Co-IP) assays

Cells were collected by scraping from plates in ice-cold phosphate-buffered saline (PBS), pelleted, and flash-frozen in liquid nitrogen.

For Western blot analysis, cell pellets were thawed on ice, resuspended to 1 mL/10 cm plate of low-salt lysis buffer (0.1 M NaCl, 25 mM HEPES, 1 mM MgCl₂, 0.2 mM EDTA, 0.5% NP-40 and protease inhibitors), with 125 U/mL of benzonase (Novagen), passed through a 25G needle, rocked at 4°C for 1 hour and a NaCl solution was added to reach a final concentration of 0.2 M. Lysates were then rocked at 4°C for 30 min and centrifuged at maximum speed at 4°C. Supernatants were quantified by Bradford. Between 15-60 µg of proteins were loaded onto 9% Bis-Tris SDS-PAGE gel, transferred onto nitrocellulose membrane (Amershan Protran 0.45µm NC) for 2 hours at 100V, blocked in TBS-Tween with 10% milk for at least 1 hour at room temperature and blotted overnight at 4°C with primary antibodies in TBS-T with 5% milk. HRP-conjugated secondary antibodies were diluted 1:5000 in TBS-T with 5% milk and incubated at room temperature for an hour.

For Co-IP experiments, cell pellets were thawed on ice, resuspended to 1 mL/10 cm plate of cell lysis buffer (5 mM PIPES pH 8.0, 85 mM KCl, 0.5% NP-40 and protease inhibitors), and incubated on ice for 10 min. Nuclei were pelleted in a tabletop centrifuge at 4°C, at 4,000 rpm for 10 min, and resuspended to 0.5 mL/10 cm plate of low salt lysis buffer with benzonase as above. For each sample, 1 mg of proteins was diluted in 1 mL of Co-IP buffer (0.2 M NaCl, 25 mM Hepes, 1 mM MgCl₂, 0.2 mM EDTA, 0.5% NP-40 and protease inhibitors), pre-cleared for 2 hours at 4°C with protein G-sepharose beads (GE Healthcare Life Sciences) before overnight immunoprecipitation with 4 µg of either normal serum IgGs or specific antibodies as listed above. Some pre-cleared lysate was kept at 4°C overnight as input. Protein G sepharose beads pre-cleared overnight in CoIP buffer with 0.5% BSA were then added to the samples and incubated at 4°C for 2 hours. After extensive washes in Co-IP buffer, proteins were eluted from the beads by boiling for 5 min in 2X SDS-loading buffer and analyzed by SDS-PAGE and Western blot.

Datasets and accession numbers

The ChIP-seq data discussed in this publication have been deposited in NCBI's Gene Expression Omnibus (Edgar et al., 2002) and are accessible through GEO Series accession number GSE90994. We

compared our ChIP-seq to previous ChIP-Seq studies of Rad21 and CTCF: (Handoko et al., 2011; Nitzsche et al., 2011; Shen et al., 2012) and GSE29218.

Fluorescence Recovery After Photobleaching (FRAP) imaging

FRAP was performed on an inverted Zeiss LSM 710 AxioObserver confocal microscope equipped with a motorized stage, a full incubation chamber maintaining 37°C/5% CO₂, a heated stage, an X-Cite 120 illumination source as well as several laser lines (only the 561 nm laser was used here). Images were acquired on a 40x Plan NeoFluar NA1.3 oil-immersion objective at a zoom corresponding to a 100 nm x 100 nm pixel size and the microscope controlled using the Zeiss Zen software. In most FRAP experiments, except where otherwise noted, 300 frames were acquired at either 1 frame per second allowing 20 frames to be acquired before the bleach pulse to accurately estimate baseline fluorescence or 330 frames at 1 frame per two seconds again allowing 20 frames to be acquired before the bleach pulse. A circular bleach spot ($r = 10$ pixels) was chosen in a region of homogenous fluorescence at a position at least 1 μm from nuclear or nucleolar boundaries. The spot was bleached using maximal laser intensity and pixel dwell time corresponding to a total bleach time of ~ 1 s. We note that because the bleach duration was relatively long compared to molecular diffusion, it is not possible to accurately estimate the bound and free fractions from our FRAP curves.

We generally collected data from 6-10 cells per cell line per condition per day and all presented data is from at least three independent replicates on different days. To quantify and drift-correct the FRAP movies (cell movement is an issue, especially for mES cells), we custom-wrote a pipeline in MATLAB. Briefly, we manually identify the bleach spot. The nucleus is automatically identified by thresholding images after Gaussian smoothing and hole-filling (to avoid the bleach spot as being identified as not belonging to the nucleus). We use an exponentially decaying (from 100% to $\sim 85\%$ of initial over one movie) threshold to account for whole-nucleus photobleaching during the time-lapse acquisition. Next, we quantify the bleach spot signal as the mean intensity of a slightly smaller circle ($r = 0.6 \mu\text{m}$), which is more robust to lateral drift. The FRAP signal is corrected for photobleaching using the measured reduction in total nuclear fluorescence ($\sim 15\%$ over 300-330 frames at the low laser intensity used after bleaching) and internally normalized to its mean value during the 20 frames before bleaching. We correct for drift by manually updating a drift vector quantifying cell movement during the experiment. Finally, drift- and photobleaching corrected FRAP curves from each single cell were averaged to generate a mean FRAP recovery. We used the mean FRAP recovery in all figures and for model-fitting.

Model selection is a crucial step in FRAP experiments and has been studied extensively (Mueller et al., 2008, 2010; Sprague et al., 2004). A full FRAP model considers both diffusion, the shape of the bleach spot and reactions (e.g. binding and unbinding). However, Sprague *et al.* identified circumstances under which simpler models are applicable (Sprague et al., 2004). Importantly, minimizing the number of fitted parameters is desirable because FRAP modeling tends to otherwise be prone to overfitting. Sprague *et al.* showed that when:

$$\frac{k_{\text{ON}}^* w^2}{D_{\text{FREE}}} \ll 1 \text{ and } \frac{k_{\text{OFF}}}{k_{\text{ON}}^*} \lesssim 1$$

Then a “reaction dominant” FRAP model is most appropriate (w is the radius of the bleach spot). In the case of the second condition, for CTCF in both mES and U2OS cells, $k_{\text{OFF}} \approx k_{\text{ON}}^*$. Likewise, for mRad21-Halo in mESCs $k_{\text{OFF}} \approx k_{\text{ON}}^*$. Thus, the second condition suggests a reaction dominant model. For the first condition, we find:

$$\text{Halo-mCTCF in mESCs: } \frac{k_{\text{ON}}^* w^2}{D_{\text{FREE}}} = \frac{0.015 \text{ s}^{-1} \cdot (0.6 \mu\text{m})^2}{2.5 \mu\text{m}^2 \text{ s}^{-1}} = 0.0022 \ll 1$$

$$\text{mRad21 in mESCs (G1 phase): } \frac{k_{\text{ON}}^* w^2}{D_{\text{FREE}}} = \frac{0.0005 \text{ s}^{-1} \cdot (0.6 \mu\text{m})^2}{1.5 \mu\text{m}^2 \text{ s}^{-1}} = 0.00012 \ll 1$$

Thus, both CTCF and Rad21 lie within the reaction dominant parameter space and a reaction dominant FRAP model is therefore the most appropriate choice. As has been demonstrated previously

(Sprague et al., 2004), in the reaction dominant parameter range, the FRAP recovery depends only on k_{OFF} and we fit the FRAP recoveries to the reaction dominant model below:

$$FRAP(t) = 1 - Ae^{-k_a t} - Be^{-k_b t}$$

After model-fitting (Figure 2–Figure Supplement 2D and 3C), we used the slower off rate to estimate the residence time according to $\tau_s = \frac{1}{k_{\text{off}}}$.

In FRAP modeling, an important question is whether or not it is justifiable to ignore diffusion (as the above model does) and the radial shape of the bleach spot. Mueller *et al.* previously showed that ignoring diffusion can lead to serious errors for typical transcription factors which show rapid FRAP recovery (in the seconds to tens of seconds range) (Mueller et al., 2008). To test whether diffusion must be taken into account we plotted the radial shape of the bleach spot as a function of time. In general, if recovery is due to binding, the recovery should be mostly uniform across the bleach area, since all binding sites are equally likely to be sampled. If on the other hand diffusion dominates the recovery, the outer edges of the circle will recover first and the center of the circle last, since unbleached molecules are diffusing in from the outside. As can be seen (Figure 2–Figure Supplement 3E), the radial profile of the bleach spot is flat and thus diffusion can be ignored in the FRAP modeling. We note that in previous studies on typical transcription factors, complete or near-complete FRAP recovery was generally observed in the 10-20 second range and here diffusion is critical (Mazza et al., 2012; Mueller et al., 2008; Sprague et al., 2004). But in the case of CTCF and cohesin, FRAP recovery is about two orders of magnitude slower and thus it is not surprising that diffusion can be ignored. Finally, Mueller *et al.* modeled the shape of the bleach spot as a Gaussian (Mueller et al., 2008), but showed that if the flat part of the bleach spot is used instead, equivalent results are obtained. Thus, in our case we bleach a circle with a 1 μm radius, but use a circle with a 0.6 μm radius to calculate the FRAP recovery, which is in the uniform area of the radial bleach profile. In addition to being equivalent to the full Gaussian description of the radial bleach profile, it has the advantage of being much more robust to cell drift, which is extensive for mES cells over the 11 min that most of our FRAP experiments last.

Finally, it came to our attention that during extended FRAP experiments (in the multi hour range) incomplete washout of Halo- or SNAP-dye can lead to artifactual FRAP recovery (Rhodes et al., 2017). This is most likely through dye binding to new protein produced after the bleach pulse. This can be corrected for by adding an excess of “dark” Halo- or SNAP-ligand, such that any newly synthesized protein binds the dark ligand. However, this is unlikely to contribute significantly to FRAP recoveries on the minute timescale since we estimate that only around 1% of the total protein is replenished during our longest FRAP experiments. Consistently, we could not detect a difference in FRAP recovery after adding excess dark ligand (Figure 2–Figure Supplement 3F). We conclude that our FRAP experiments were not affected by this.

Appendix 1

Estimation of the fraction of CTCF and cohesin molecules involved in looping

Since both CTCF and cohesin have functions beyond regulating chromatin looping, an important question is which fraction of chromatin-bound CTCF and cohesin sites are involved in chromatin looping. Conventionally, the number of occupied binding sites are assessed using ChIP-Seq and identified as peaks significantly above a background threshold. Experimentally, a spectrum of binding enrichments is always observed and peak calling involves a somewhat arbitrary discretization step. Using MACS2 (Zhang et al., 2008) and standard parameters (Materials and Methods), we call 68,077 CTCF ChIP-Seq peaks in wild-type mESCs and a similar number in Halo-mCTCF knock-in cells (C59; see Supplementary File 1 for full details). Likewise, for cohesin we observe 33,434 ChIP-Seq peaks of which 97% of the peaks overlap with a CTCF peaks. Thus, the cohesin peaks appear to be a subset of CTCF peaks and there appears to be significant cohesin binding at many other CTCF peaks, albeit below the peak-calling threshold.

What fraction of CTCF/cohesin sites are involved in looping? As for calling peaks using ChIP-Seq data, loops are also generally called by thresholding Hi-C data and appear as corner-peaks in the Hi-C interaction matrix. Different groups have used different thresholds and Hi-C data at different resolutions and accordingly have reported different numbers of loops (Jin et al., 2013; Rao et al., 2014; Sanyal et al., 2012). The highest resolution Hi-C data published to date is from Rao *et al.* and they report ~10,000 loops using a very stringent and conservative loop-calling algorithm in GM12878 cells (Rao et al., 2014). The same group called substantially fewer loops in other cell lines sequenced at a lower sequencing depth (lower resolution Hi-C). However, using a method called Aggregate Peak Analysis (APA), which allows Hi-C maps at different resolutions to be compared, Rao *et al.* found that the fewer loops were due to the lower sequencing depth rather than an absence of loops in these cell lines. In fact, they found that loops were largely conserved between different cell lines and between human and mouse cells. Thus, it seems like the ability to call loops depends on sequencing depth and thus, it seems likely that in the future when even higher resolution Hi-C data may be available, the number of high-confidence loops will significantly exceed 10,000. According to Rao *et al.*, almost all Hi-C loops are anchored by both CTCF and cohesin. Thus, a lower bound estimate would be that ~20,000 CTCF and Cohesin ChIP-Seq sites anchor loops. However, as also pointed out by Rao *et al.* and clearly illustrated in Figure 2 of an informative recent review by Merkenschlager and Nora (Merkenschlager and Nora, 2016), many loops appear to be anchored by clusters of CTCF/cohesin binding sites. Thus, since multiple CTCF and cohesin ChIP-Seq sites can anchor the same loop, 20,000 seems to be too low a bound. If we further take into account that future Hi-C studies, which achieve even greater resolution, will likely call even more loops, it seems reasonably conservative to take ~25,000 CTCF and cohesin ChIP-Seq peaks as the number of peaks involved in looping. While this is clearly a rough and somewhat speculative estimate, if we compare this to the MACS2-called ChIP-seq peaks we find that ~25,000/68,077 or ~37% of CTCF ChIP-Seq called binding sites and ~25,000/33,434 or ~75% of cohesin ChIP-Seq called binding sites are involved in chromatin looping. In the main text of the manuscript, we refer to this as around one-third of CTCF sites and as a majority of cohesin sites. We also note that within the extrusion model, a significant fraction of cohesin molecules that are topologically engaged on chromatin may be actively travelling across the chromosome (i.e. “extruding”) and this fraction is unlikely to be picked up by any ChIP-Seq peak-calling analysis. This fraction would appear indistinguishable from cohesin molecules bound at specific loop boundaries in our FRAP analysis. Nevertheless, among cohesin molecules that remain at a specific location for an extended period, i.e. the fraction likely to result in ChIP-Seq peaks, the majority appears around loop boundaries.

For CTCF sites, we would also like to note that the CTCF sites involved in looping tend to be the ones with the highest ChIP-Seq enrichment (Merkenschlager and Nora, 2016). The ChIP-Seq enrichment should be approximately proportional to the fraction of time the binding site is occupied. Thus, the CTCF sites that make up loop anchors are likely bound a higher fraction of the time than

other CTCF sites. This is important, because the probability of observing CTCF binding to a particular site in our imaging experiments should also scale with the fractional occupancy of this site. Thus, in our single-molecule tracking experiments (Figure 2A-D), we are over-sampling precisely the CTCF binding events at loop anchors. Thus, most likely, of the binding events that we observe in Figure 2A-D, >37% are involved in looping. Further support for this interpretation, comes from the observation that overexpressing CTCF greatly increases the rate of FRAP recovery (Figure 2-Figure Supplement 2B: black curve vs. red and blue curves). The simplest explanation for this over-expression artefact is that when the abundance of CTCF substantially increases, many CTCF molecules now start binding “poor” CTCF sites on chromatin and accordingly the apparent residence time is decreased. For these reasons, we believe that our estimate that around one-third of CTCF sites are involved in looping is a very conservative estimate and we believe that this is a lower bound.

In the case of cohesin, cohesin clearly has many other functions besides looping such as sister chromatids cohesion and DNA repair through homologous recombination. However, most of these functions only exist from S-phase to division during the cell cycle. Thus, our estimate that a majority of cohesin molecules are involved in chromatin looping apply to G1-phase, where sister chromatid cohesion and homologous recombination does not occur.

Moreover, we note that both ChIP-Seq and Hi-C and the other 3C variants (e.g. 4C and 5C) all provides snapshots of large cell populations. Thus, a ChIP-Seq peak and a Hi-C loop shows that a binding site is occupied and that a loop exists, in a fraction of cells, but it is extremely difficult to estimate how big this fraction is from these techniques. And even with DNA FISH measurements, it can be difficult to ascertain precisely the frequency with which a loop occurs in a cells (Fudenberg and Imakaev, 2016). A very recent paper used single-cell Hi-C to estimate that loops form in 62.1% of mouse ES cells (Stevens et al., 2017). This is a somewhat higher estimate than what most DNA-FISH studies find. Nevertheless, if we assume that the fractional occupancy of CTCF sites is significantly less than 62.1%, which is likely the case (but cannot be determined with knowing the absolute number of CTCF molecules per cell), this would also imply that a much higher fraction than 37% of CTCF binding sites is involved in looping. However, because we do not yet have good data on the fractional binding site occupancy and on the exact number and frequency of loops, it is difficult to say with certainty what fraction of CTCF molecules are truly involved in looping.

Finally, we note that if loops are formed by a cohesin-mediated extrusion mechanism (Fudenberg et al., 2016; Sanborn et al., 2015), many cohesin molecules will be actively extruding loop and thus involved in looping, but not actually show up in ChIP-Seq as a peak. This is because for the extrusion model to work, cohesin has to extrude quite quickly along chromatin and thus its occupancy is effectively “spread out” and will not show up in a ChIP-Seq experiment as a peak and thus will not be called. This may be one reason, why we find more CTCF ChIP-Seq peaks than cohesin peaks. Thus, it is very plausible that more cohesin than CTCF molecules will be chromatin associated even though fewer cohesin ChIP-Seq peaks are called.

References

- Andrey, G., Schöpflin, R., Jerković, I., Heinrich, V., Ibrahim, D.M., Paliou, C., Hochradel, M., Timmermann, B., Haas, S., Vingron, M., et al. (2016). Characterization of hundreds of regulatory landscapes in developing limbs reveals two regimes of chromatin folding. *Genome Res.* .
- Benedetti, F., Dorier, J., Burnier, Y., and Stasiak, A. (2014). Models that include supercoiling of topological domains reproduce several known features of interphase chromosomes. *Nucleic Acids Res.* *42*, 2848–2855.
- Blankenberg, D., Kuster, G. Von, Coraor, N., Ananda, G., Lazarus, R., Mangan, M., Nekrutenko, A., and Taylor, J. (2010). Galaxy: A web-based genome analysis tool for experimentalists. *Curr. Protoc. Mol. Biol.*
- Boettiger, A.N., Bintu, B., Moffitt, J.R., Wang, S., Beliveau, B.J., Fudenberg, G., Imakaev, M., Mirny, L.A., Wu, C., and Zhuang, X. (2016). Super-resolution imaging reveals distinct chromatin folding for different epigenetic states. *Nature* *529*, 418–422.
- Chen, J., Zhang, Z., Li, L., Chen, B.C., Revyakin, A., Hajj, B., Legant, W., Dahan, M., Lionnet, T., Betzig, E., et al. (2014). Single-molecule dynamics of enhanceosome assembly in embryonic stem cells. *Cell* *156*, 1274–1285.
- Davidson, I.F., Goetz, D., Zaczek, M.P., Molodtsov, M.I., Huis in ’t Veld, P.J., Weissmann, F., Litos, G., Cisneros, D.A., Ocampo-Hafalla, M., Ladurner, R., et al. (2016). Rapid movement and transcriptional re-localization of human cohesin on DNA. *EMBO J.*
- Dekker, J., and Mirny, L. (2016). The 3D Genome as Moderator of Chromosomal Communication. *Cell* *164*, 1110–1121.
- Dixon, J.R., Selvaraj, S., Yue, F., Kim, A., Li, Y., Shen, Y., Hu, M., Liu, J.S., and Ren, B. (2012). Topological domains in mammalian genomes identified by analysis of chromatin interactions. *Nature* *485*, 376–380.
- Edgar, R., Domrachev, M., and Lash, A.E. (2002). Gene Expression Omnibus: NCBI gene expression and hybridization array data repository.
- Elf, J., Li, G.-W., and Xie, X.S. (2007). Probing transcription factor dynamics at the single-molecule level in a living cell. *Science* *316*, 1191–1194.
- Elmokadem, A., and Yu, J. (2015). Optimal Drift Correction for Superresolution Localization Microscopy with Bayesian Inference. *Biophys. J.* *109*, 1772–1780.
- Flavahan, W.A., Drier, Y., Liao, B.B., Gillespie, S.M., Venteicher, A.S., Stemmer-Rachamimov, A.O., Suvà, M.L., and Bernstein, B.E. (2015). Insulator dysfunction and oncogene activation in IDH mutant gliomas. *Nature* *529*, 110–114.
- Fudenberg, G., and Imakaev, M. (2016). FISH-ing for captured contacts: towards reconciling FISH and 3C. *bioRxiv*.
- Fudenberg, G., Imakaev, M., Lu, C., Goloborodko, A., Abdennur, N., and Mirny, L.A. (2016). Formation of Chromosomal Domains by Loop Extrusion. *Cell Rep.* *15*, 2038–2049.
- Gerlich, D., Koch, B., Dupeux, F., Peters, J.-M., and Ellenberg, J. (2006). Live-Cell Imaging Reveals a Stable Cohesin-Chromatin Interaction after but Not before DNA Replication. *Curr. Biol.* *16*, 1571–1578.
- Ghirlando, R., and Felsenfeld, G. (2016). CTCF: Making the right connections. *Genes Dev.* *30*, 881–891.

1507 Giardine, B., Riemer, C., Hardison, R.C., Burhans, R., Elnitski, L., Shah, P., Zhang, Y., Blankenberg,
 1508 D., Albert, I., Taylor, J., et al. (2005). Galaxy: A platform for interactive large-scale genome analysis.
 1509 *Genome Res.* *15*, 1451–1455.

1510 Giorgetti, L., Galupa, R., Nora, E.P., Piolot, T., Lam, F., Dekker, J., Tiana, G., and Heard, E. (2014).
 1511 Predictive polymer modeling reveals coupled fluctuations in chromosome conformation and
 1512 transcription. *Cell* *157*, 950–963.

1513 Goecks, J., Nekrutenko, A., and Taylor, J. (2010). Galaxy: a comprehensive approach for supporting
 1514 accessible, reproducible, and transparent computational research in the life sciences. *Genome Biol.* *11*,
 1515 R86.

1516 Grimm, J.B., English, B.P., Chen, J., Slaughter, J.P., Zhang, Z., Revyakin, A., Patel, R., Macklin, J.J.,
 1517 Normanno, D., Singer, R.H., et al. (2015). A general method to improve fluorophores for live-cell and
 1518 single-molecule microscopy. *Nat. Methods* *12*, 244–250.

1519 Grimm, J.B., English, B.P., Choi, H., Muthusamy, A.K., Mehl, B.P., Dong, P., Brown, T.A., Lippincott-
 1520 Schwartz, J., Liu, Z., Lionnet, T., et al. (2016). Bright photoactivatable fluorophores for single-molecule
 1521 imaging. *Nat. Methods* 66779.

1522 Guo, Y., Xu, Q., Canzio, D., Shou, J., Li, J., Gorkin, D.U., Jung, I., Wu, H., Zhai, Y., Tang, Y., et al.
 1523 (2015). CRISPR Inversion of CTCF Sites Alters Genome Topology and Enhancer/Promoter Function.
 1524 *Cell* *162*, 900–910.

1525 Haering, C.H., Schoffnegger, D., Nishino, T., Helmhart, W., Nasmyth, K., and Löwe, J. (2004).
 1526 Structure and stability of cohesin’s Smc1-kleisin interaction. *Mol. Cell* *15*, 951–964.

1527 Handoko, L., Xu, H., Li, G., Ngan, C.Y., Chew, E., Schnapp, M., Lee, C.W.H., Ye, C., Ping, J.L.H.,
 1528 Mulawadi, F., et al. (2011). CTCF-mediated functional chromatin interactome in pluripotent cells. *Nat.*
 1529 *Genet.* *43*, 630–638.

1530 Hnisz, D., Weintraub, A.S., Day, D.S., Valton, A., Bak, R.O., Li, C.H., Goldmann, J., Lajoie, B.R., Fan,
 1531 Z.P., Sigova, A.A., et al. (2016a). Activation of proto-oncogenes by disruption of chromosome
 1532 neighborhoods. *Science* (80-.). *351*, 1454–1458.

1533 Hnisz, D., Day, D.S., and Young, R.A. (2016b). Insulated Neighborhoods: Structural and Functional
 1534 Units of Mammalian Gene Control. *Cell* *167*, 1188–1200.

1535 Hu, J., Zhang, Y., Zhao, L., Frock, R.L., Du, Z., Meyers, R.M., Meng, F.L., Schatz, D.G., and Alt, F.W.
 1536 (2015). Chromosomal Loop Domains Direct the Recombination of Antigen Receptor Genes. *Cell* *163*,
 1537 947–959.

1538 Huis in ’t Veld, P.J., Herzog, F., Ladurner, R., Davidson, I.F., Piric, S., Kreidl, E., Bhaskara, V.,
 1539 Aebersold, R., Peters, J.-M., Huis, P.J., et al. (2014). Characterization of a DNA exit gate in the human
 1540 cohesin ring. *Science* *346*, 968–972.

1541 Ivanov, D., and Nasmyth, K. (2005). A Topological Interaction between Cohesin Rings and a Circular
 1542 Minichromosome. *Cell* *122*, 849–860.

1543 Jin, F., Li, Y., Dixon, J.R., Selvaraj, S., Ye, Z., Lee, A.Y., Yen, C.-A., Schmitt, A.D., Espinoza, C.A., and
 1544 Ren, B. (2013). A high-resolution map of the three-dimensional chromatin interactome in human cells.
 1545 *Nature* *503*, 290–294.

1546 Kues, T., and Kubitscheck, U. (2002). Single molecule motion perpendicular to the focal plane of a
 1547 microscope: Application to splicing factor dynamics within the cell nucleus. *Single Mol.* *3*, 218–224.

1548 Langmead, B., Trapnell, C., Pop, M., and Salzberg, S.L. (2009). Ultrafast and memory-efficient
 1549 alignment of short DNA sequences to the human genome. *Genome Biol.* *10*, R25.

1550 Lengronne, A., Katou, Y., Mori, S., Yokobayashi, S., Kelly, G.P., Itoh, T., Watanabe, Y., Shirahige, K.,
1551 and Uhlmann, F. (2004). Cohesin relocation from sites of chromosomal loading to places of convergent
1552 transcription. *Nature* *430*, 573–578.

1553 Lupianez, D.G., Kraft, K., Heinrich, V., Krawitz, P., Brancati, F., Klopocki, E., Horn, D., Kayserili, H.,
1554 Opitz, J.M., Laxova, R., et al. (2015). Disruptions of topological chromatin domains cause pathogenic
1555 rewiring of gene-enhancer interactions. *Cell* *161*, 1012–1025.

1556 Manley, S., Gillette, J.M., Patterson, G.H., Shroff, H., Hess, H.F., Betzig, E., and Lippincott-Schwartz,
1557 J. (2008). High-density mapping of single-molecule trajectories with photoactivated localization
1558 microscopy. *Nat. Methods* *5*, 155–157.

1559 Matsuoka, S., Shibata, T., and Ueda, M. (2009). Statistical analysis of lateral diffusion and multistate
1560 kinetics in single-molecule imaging. *Biophys. J.* *97*, 1115–1124.

1561 Mazza, D., Abernathy, A., Golob, N., Morisaki, T., and McNally, J.G. (2012). A benchmark for
1562 chromatin binding measurements in live cells. *Nucleic Acids Res.* *40*.

1563 Merckenschlager, M., and Nora, E.P. (2016). CTCF and Cohesin in Genome Folding and
1564 Transcriptional Gene Regulation. *Annu. Rev. Genomics Hum. Genet.* 1–27.

1565 Mirny, L., Slutsky, M., Wunderlich, Z., Tafvizi, A., Leith, J., and Kosmrlj, A. (2009). How a protein
1566 searches for its site on DNA: the mechanism of facilitated diffusion. *J. Phys. A Math. Theor.* *42*,
1567 434013.

1568 Mueller, F., Wach, P., and McNally, J.G. (2008). Evidence for a common mode of transcription factor
1569 interaction with chromatin as revealed by improved quantitative fluorescence recovery after
1570 photobleaching. *Biophys. J.* *94*, 3323–3339.

1571 Mueller, F., Mazza, D., Stasevich, T.J., and McNally, J.G. (2010). FRAP and kinetic modeling in the
1572 analysis of nuclear protein dynamics: what do we really know? *Curr. Op. Cell Biol.* *22*, 403–411.

1573 Nakahashi, H., Kwon, K.R.K., Resch, W., Vian, L., Dose, M., Stavreva, D., Hakim, O., Pruett, N.,
1574 Nelson, S., Yamane, A., et al. (2013). A Genome-wide Map of CTCF Multivalency Redefines the CTCF
1575 Code. *Cell Rep.* *3*, 1678–1689.

1576 Nasmyth, K. (2001). Disseminating the Genome: Joining, Resolving, and Separating Sister Chromatids
1577 During Mitosis and Meiosis. *Annu. Rev. Genet.* *35*, 673–745.

1578 Naumova, N., Imakaev, M., Fudenberg, G., Zhan, Y., Lajoie, B.R., Mirny, L.A., and Dekker, J. (2013).
1579 Organization of the mitotic chromosome. *Science* *342*, 948–953.

1580 Nitzsche, A., Paszkowski-Rogacz, M., Matarese, F., Janssen-Megens, E.M., Hubner, N.C., Schulz, H.,
1581 de Vries, I., Ding, L., Huebner, N., Mann, M., et al. (2011). RAD21 cooperates with pluripotency
1582 transcription factors in the maintenance of embryonic stem cell identity. *PLoS One* *6*.

1583 Nora, E.P., Lajoie, B.R., Schulz, E.G., Giorgetti, L., Okamoto, I., Servant, N., Piolot, T., van Berkum,
1584 N.L., Meisig, J., Sedat, J., et al. (2012). Spatial partitioning of the regulatory landscape of the X-
1585 inactivation centre. *Nature* *485*, 381–385.

1586 Nora, E.P., Goloborodko, A., Valton, A.-L., Gibcus, J., Uebbersohn, A., Abdennur, N., Dekker, J.,
1587 Mirny, L., and Bruneau, B. (2016). Targeted degradation of CTCF decouples local insulation of
1588 chromosome domains from higher-order genomic compartmentalization. *bioRxiv*.

1589 Normanno, D., Boudarène, L., Dugast-Darzacq, C., Chen, J., Richter, C., Proux, F., Bénichou, O.,
1590 Voituriez, R., Darzacq, X., and Dahan, M. (2015). Probing the target search of DNA-binding proteins
1591 in mammalian cells using TetR as model searcher. *Nat. Commun.* *6*, 7357.

1592 Parelho, V., Hadjur, S., Spivakov, M., Leleu, M., Sauer, S., Gregson, H.C., Jarmuz, A., Canzonetta, C.,

1593 Webster, Z., Nesterova, T., et al. (2008). Cohesins Functionally Associate with CTCF on Mammalian
1594 Chromosome Arms. *Cell* *132*, 422–433.

1595 Pettitt, S.J., Liang, Q., Rairdan, X.Y., Moran, J.L., Prosser, H.M., Beier, D.R., Lloyd, K.C., Bradley, A.,
1596 and Skarnes, W.C. (2009). Agouti C57BL/6N embryonic stem cells for mouse genetic resources. *Nat.*
1597 *Methods* *6*, 493–495.

1598 Ramirez, F., Ryan, D.P., Gruning, B., Bhardwaj, V., Kilpert, F., Richter, A.S., Heyne, S., Dundar, F.,
1599 and Manke, T. (2016). deepTools2: a next generation web server for deep-sequencing data analysis.
1600 *Nucleic Acids Res.* *44*, 160–165.

1601 Ran, F.A., Hsu, P.D., Wright, J., Agarwala, V., Scott, D.A., and Zhang, F. (2013). Genome engineering
1602 using the CRISPR-Cas9 system. *Nat. Protoc.* *8*, 2281–2308.

1603 Rao, S.S.P., Huntley, M.H., Durand, N.C., Stamenova, E.K., Bochkov, I.D., Robinson, J.T., Sanborn,
1604 A.L., Machol, I., Omer, A.D., Lander, E.S., et al. (2014). A 3D map of the human genome at kilobase
1605 resolution reveals principles of chromatin looping. *Cell* *159*, 1665–1680.

1606 Rhodes, J., Haarhuis, J., Grimm, J., Rowland, B., Lavis, L., and Nasmyth, K. (2017). Cohesin Can
1607 Remain Associated With Chromosomes During DNA Replication. *bioRxiv*.

1608 Robinson, J.T., Thorvaldsdóttir, H., Winckler, W., Guttman, M., Lander, E.S., Getz, G., and Mesirov,
1609 J.P. (2011). Integrative genomics viewer. *Nat. Biotechnol.* *29*, 24–26.

1610 Rubin-Delanchy, P., Burn, G.L., Griffié, J., Williamson, D.J., Heard, N.A., Cope, A.P., and Owen, D.M.
1611 (2015). Bayesian cluster identification in single-molecule localization microscopy data. *Nat. Methods* *12*,
1612 1072–1076.

1613 Sakaue-Sawano, A., Kurokawa, H., Morimura, T., Hanyu, A., Hama, H., Osawa, H., Kashiwagi, S.,
1614 Fukami, K., Miyata, T., Miyoshi, H., et al. (2008). Visualizing Spatiotemporal Dynamics of Multicellular
1615 Cell-Cycle Progression. *Cell* *132*, 487–498.

1616 Sanborn, A.L., Rao, S.S.P., Huang, S.-C., Durand, N.C., Huntley, M.H., Jewett, A.I., Bochkov, I.D.,
1617 Chinnappan, D., Cutkosky, A., Li, J., et al. (2015). Chromatin extrusion explains key features of loop
1618 and domain formation in wild-type and engineered genomes. *Proc. Natl. Acad. Sci.* *112*, 201518552.

1619 Sanyal, A., Lajoie, B.R., Jain, G., and Dekker, J. (2012). The long-range interaction landscape of gene
1620 promoters. *Nature* *489*, 109–113.

1621 Schwarzer, W., Abdennur, N., Goloborodko, A., Pekowska, A., Fudenberg, G., Loe-Mie, Y., Fonseca,
1622 N.A., Huber, W., Haering, C., Mirny, L., et al. (2016). Two independent modes of chromosome
1623 organization are revealed by cohesin removal. *bioRxiv*.

1624 Sergé, A., Bertaux, N., Rigneault, H., and Marguet, D. (2008). Dynamic multiple-target tracing to probe
1625 spatiotemporal cartography of cell membranes. *Nat. Methods* *5*, 687–694.

1626 Sheff, M.A., and Thorn, K.S. (2004). Optimized cassettes for fluorescent protein tagging in
1627 *Saccharomyces cerevisiae*. *Yeast* *21*, 661–670.

1628 Shen, Y., Yue, F., McCleary, D.F., Ye, Z., Edsall, L., Kuan, S., Wagner, U., Dixon, J., Lee, L.,
1629 Lobanenko, V. V., et al. (2012). A map of the cis-regulatory sequences in the mouse genome. *Nature*
1630 *488*, 116–120.

1631 Skibbens, R. V. (2016). Of Rings and Rods: Regulating Cohesin Entrapment of DNA to Generate
1632 Intra- and Intermolecular Tethers. *PLoS Genet.* *12*, e1006337.

1633 Sladitschek, H.L., and Neveu, P.A. (2015). MXS-Chaining: A Highly Efficient Cloning Platform for
1634 Imaging and Flow Cytometry Approaches in Mammalian Systems. *PLoS One* *10*, e0124958.

1635 Sprague, B.L., Pego, R.L., Stavreva, D.A., and McNally, J.G. (2004). Analysis of Binding Reactions by
1636 Fluorescence Recovery after Photobleaching. *Biophys. J.* *86*, 3473–3495.

1637 Stevens, T.J., Lando, D., Basu, S., Atkinson, L.P., Cao, Y., Lee, S.F., Leeb, M., Wohlfahrt, K.J.,
1638 Boucher, W., O’Shaughnessy-Kirwan, A., et al. (2017). 3D structures of individual mammalian genomes
1639 studied by single-cell Hi-C. *Nature advance on*.

1640 Stigler, J., Çamdere, G., Koshland, D.E., and Greene, E.C. (2016). Single-Molecule Imaging Reveals a
1641 Collapsed Conformational State for DNA-Bound Cohesin. *Cell Rep.* *15*, 988–998.

1642 Stone, M.B., and Veatch, S.L. (2015). Steady-state cross-correlations for live two-colour super-
1643 resolution localization data sets. *Nat. Commun.* *6*, 7347.

1644 Testa, A., Donati, G., Yan, P., Romani, F., Huang, T.H.M., Viganò, M.A., and Mantovani, R. (2005).
1645 Chromatin immunoprecipitation (ChIP) on chip experiments uncover a widespread distribution of NF-
1646 Y binding CCAAT sites outside of core promoters. *J. Biol. Chem.* *280*, 13606–13615.

1647 Teves, S.S., An, L., Hansen, A.S., Xie, L., Darzacq, X., and Tjian, R. (2016). A dynamic mode of mitotic
1648 bookmarking by transcription factors. *Elife* *5*.

1649 Thorvaldsdóttir, H., Robinson, J.T., and Mesirov, J.P. (2013). Integrative Genomics Viewer (IGV):
1650 High-performance genomics data visualization and exploration. *Brief. Bioinform.* *14*, 178–192.

1651 Tokunaga, M., Imamoto, N., and Sakata-Sogawa, K. (2008). Highly inclined thin illumination enables
1652 clear single-molecule imaging in cells. *Nat. Methods* *5*, 159–161.

1653 Wang, S., Su, J.-H., Beliveau, B.J., Bintu, B., Moffitt, J.R., Wu, C. -t., and Zhuang, X. (2016). Spatial
1654 organization of chromatin domains and compartments in single chromosomes. *Science (80-.)*. *353*,
1655 598–602.

1656 Wang, Y., Schnitzbauer, J., Hu, Z., Li, X., Cheng, Y., Huang, Z.-L., and Huang, B. (2014). Localization
1657 events-based sample drift correction for localization microscopy with redundant cross-correlation
1658 algorithm. *Opt. Express* *22*, 15982–15991.

1659 Wendt, K.S., Yoshida, K., Itoh, T., Bando, M., Koch, B., Schirghuber, E., Tsutsumi, S., Nagae, G.,
1660 Ishihara, K., Mishiho, T., et al. (2008). Cohesin mediates transcriptional insulation by CCCTC-binding
1661 factor. *Nature* *451*, 796–801.

1662 Williamson, I., Berlivet, S., Eskeland, R., Boyle, S., Illingworth, R.S., Paquette, D., Dostie, J., and
1663 Bickmore, W.A. (2014). Spatial genome organization: Contrasting views from chromosome
1664 conformation capture and fluorescence in situ hybridization. *Genes Dev.* *28*, 2778–2791.

1665 de Wit, E., Vos, E.S.M., Holwerda, S.J.B., Valdes-Quezada, C., Verstegen, M.J.A.M., Teunissen, H.,
1666 Splinter, E., Wijchers, P.J., Krijger, P.H.L., and de Laat, W. (2015). CTCF Binding Polarity Determines
1667 Chromatin Looping. *Mol. Cell* *60*, 676–684.

1668 Yeung, C., Shtrahman, M., and Wu, X. (2007). Stick-and-diffuse and caged diffusion: a comparison of
1669 two models of synaptic vesicle dynamics. *Biophys. J.* *92*, 2271–2280.

1670 Young, L., Sung, J., Stacey, G., and Masters, J.R. (2010). Detection of Mycoplasma in cell cultures. *Nat.*
1671 *Protoc.* *5*, 929–934.

1672 Zhang, Y., Liu, T., Meyer, C.A., Eeckhoutte, J., Johnson, D.S., Bernstein, B.E., Nussbaum, C., Myers,
1673 R.M., Brown, M., Li, W., et al. (2008). Model-based analysis of ChIP-Seq (MACS). *Genome Biol* *9*,
1674 R137.

Figure 1

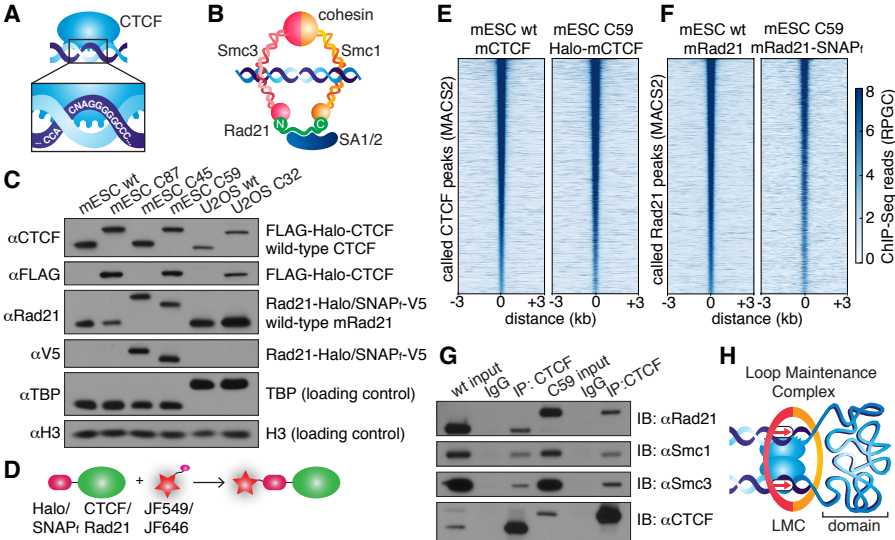


Figure 1 - Figure Supplement 1

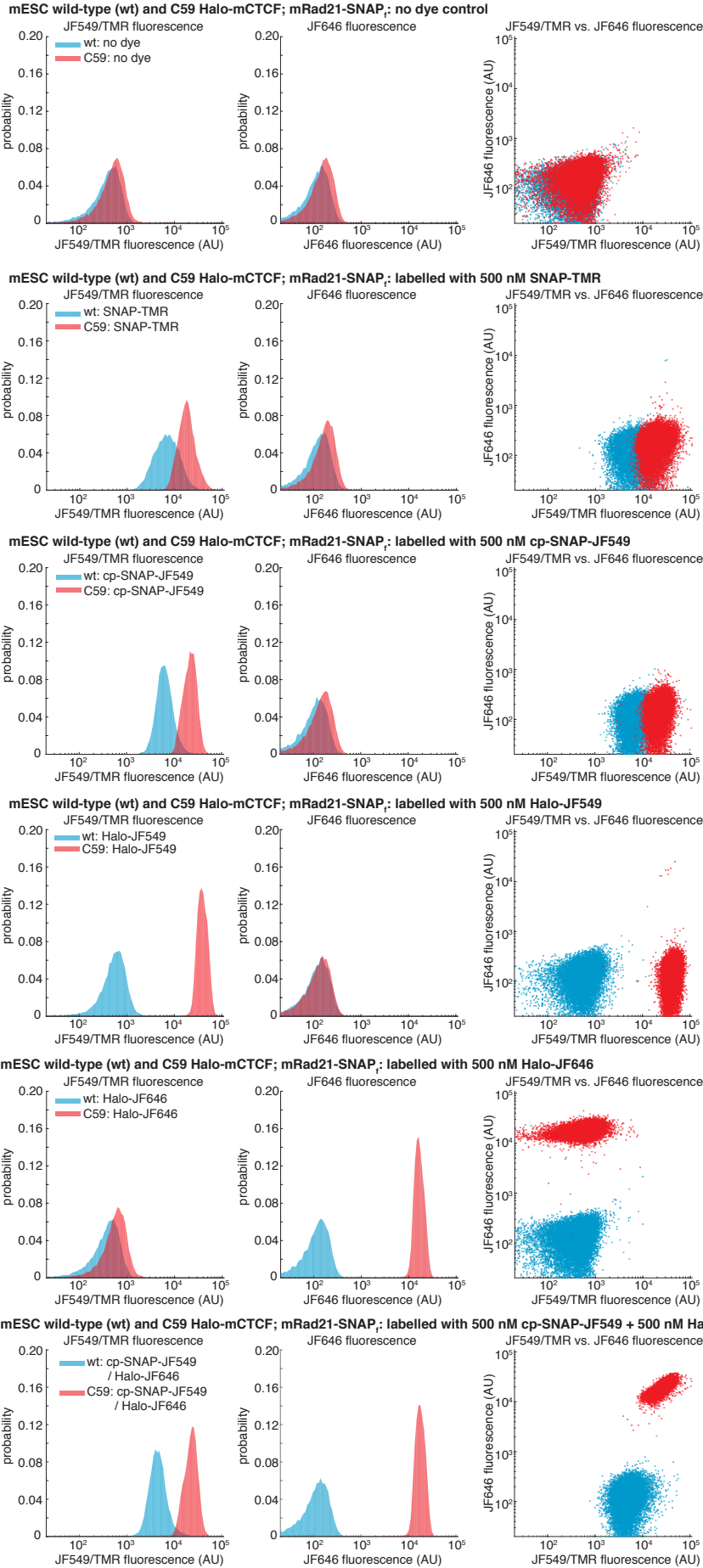


Figure 1 - Figure Supplement 2

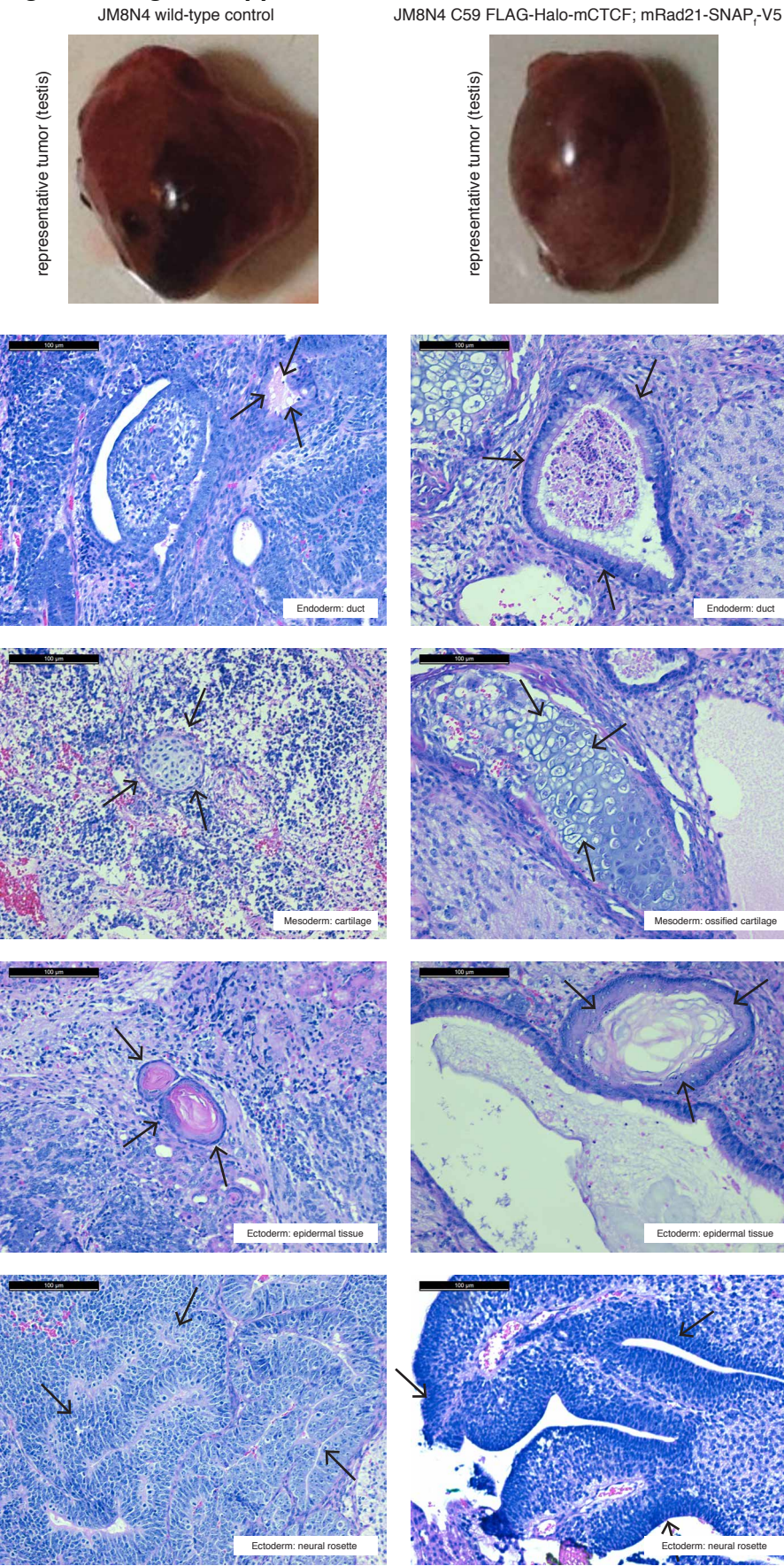


Figure 1 - Figure Supplement 3

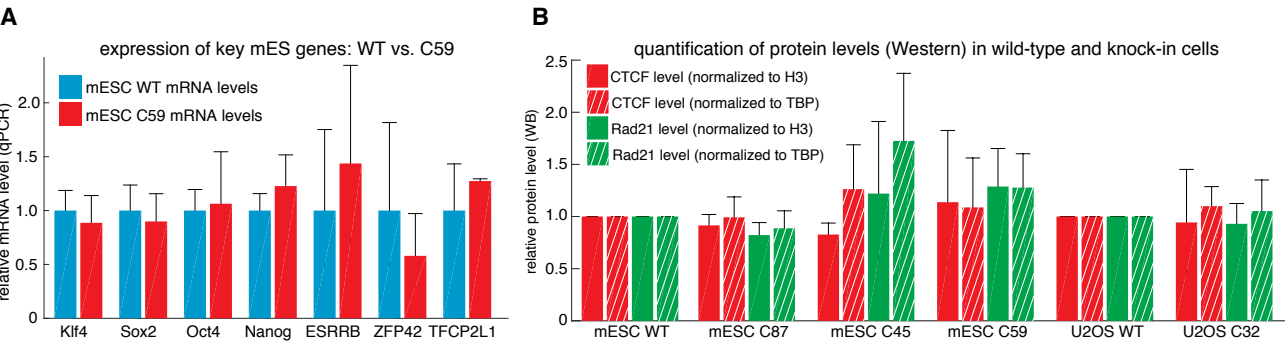


Figure 1 - Figure Supplement 4

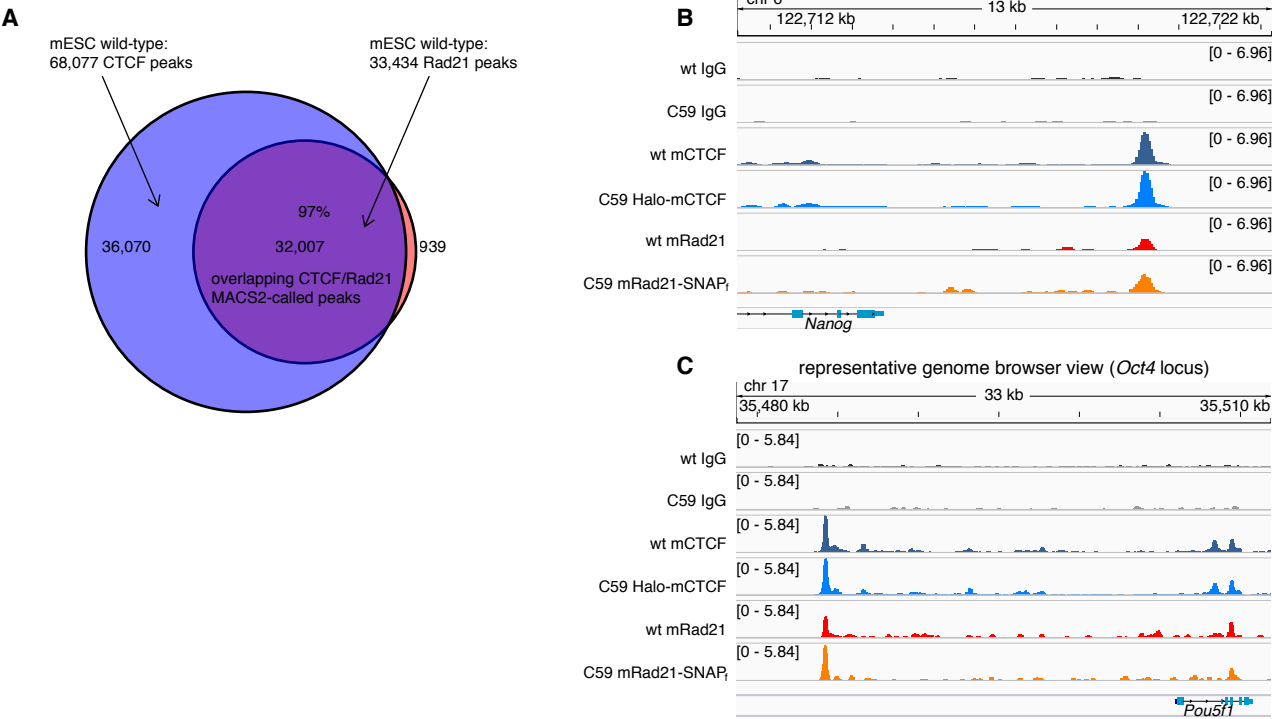


Figure 1 - Figure Supplement 5

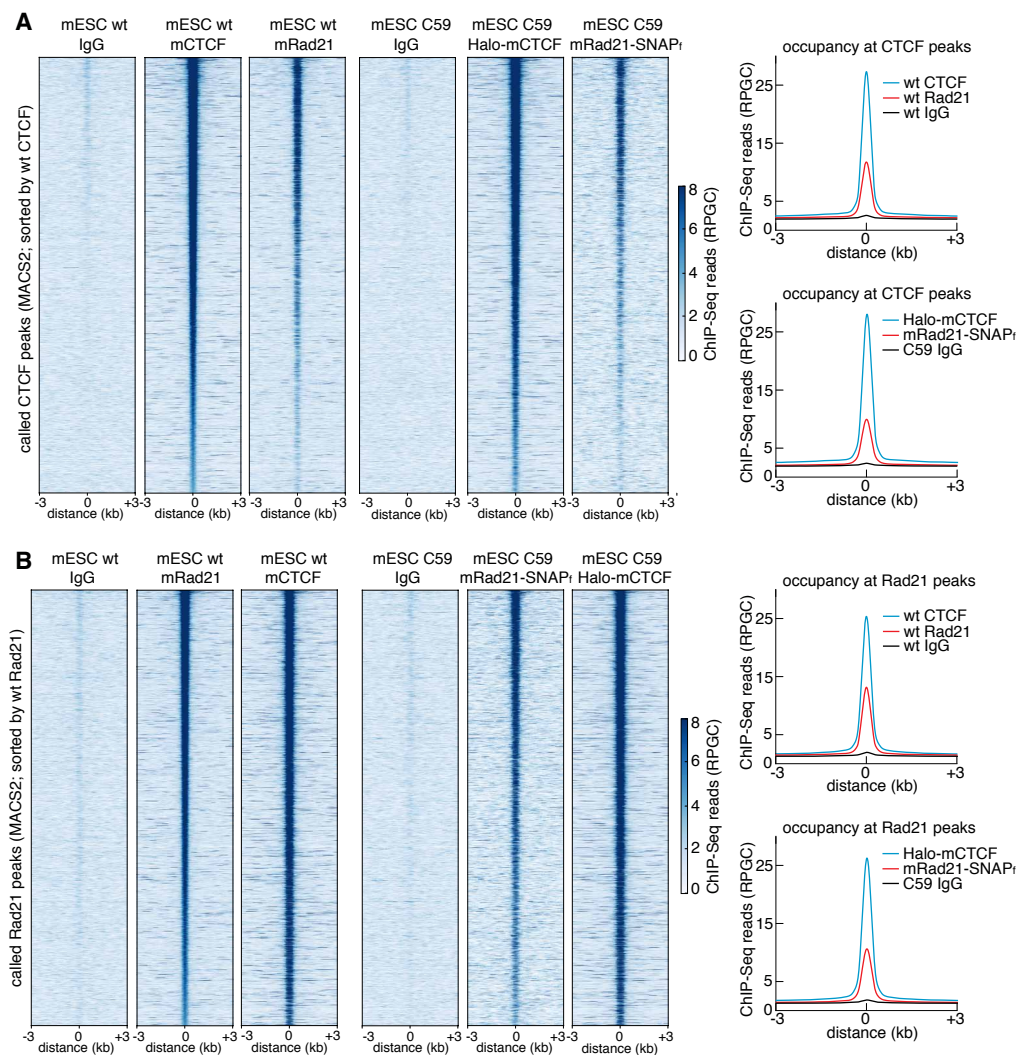


Figure 2

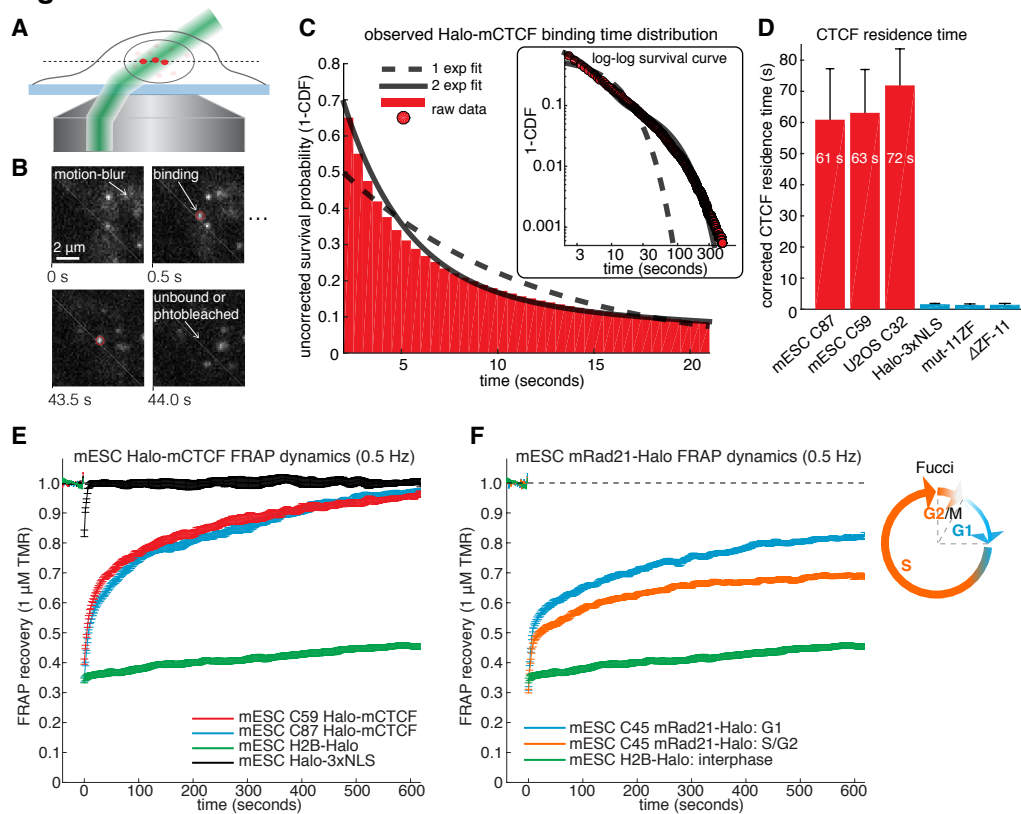


Figure 2 - Figure Supplement 1

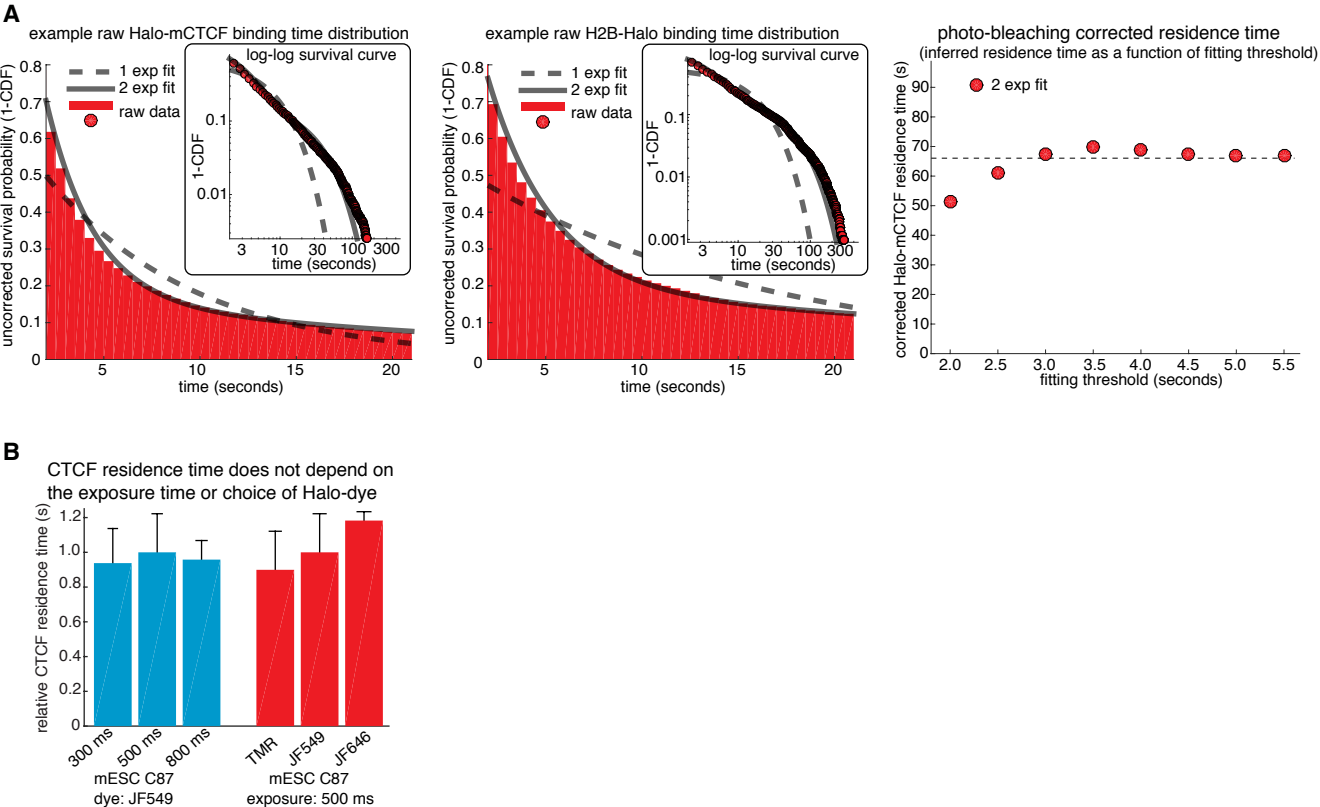


Figure 2 - Figure Supplement 2

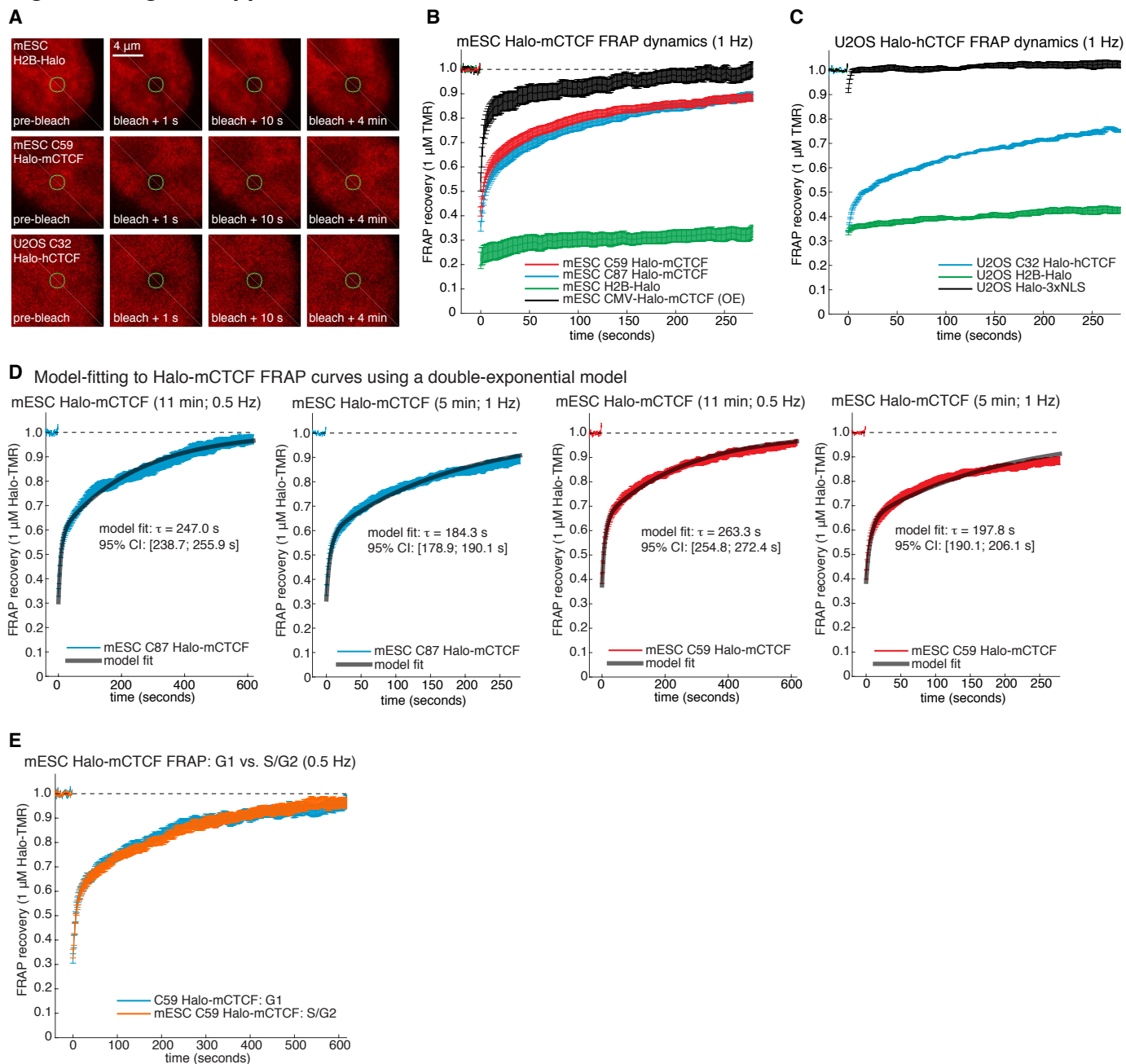


Figure 2 - Figure Supplement 3

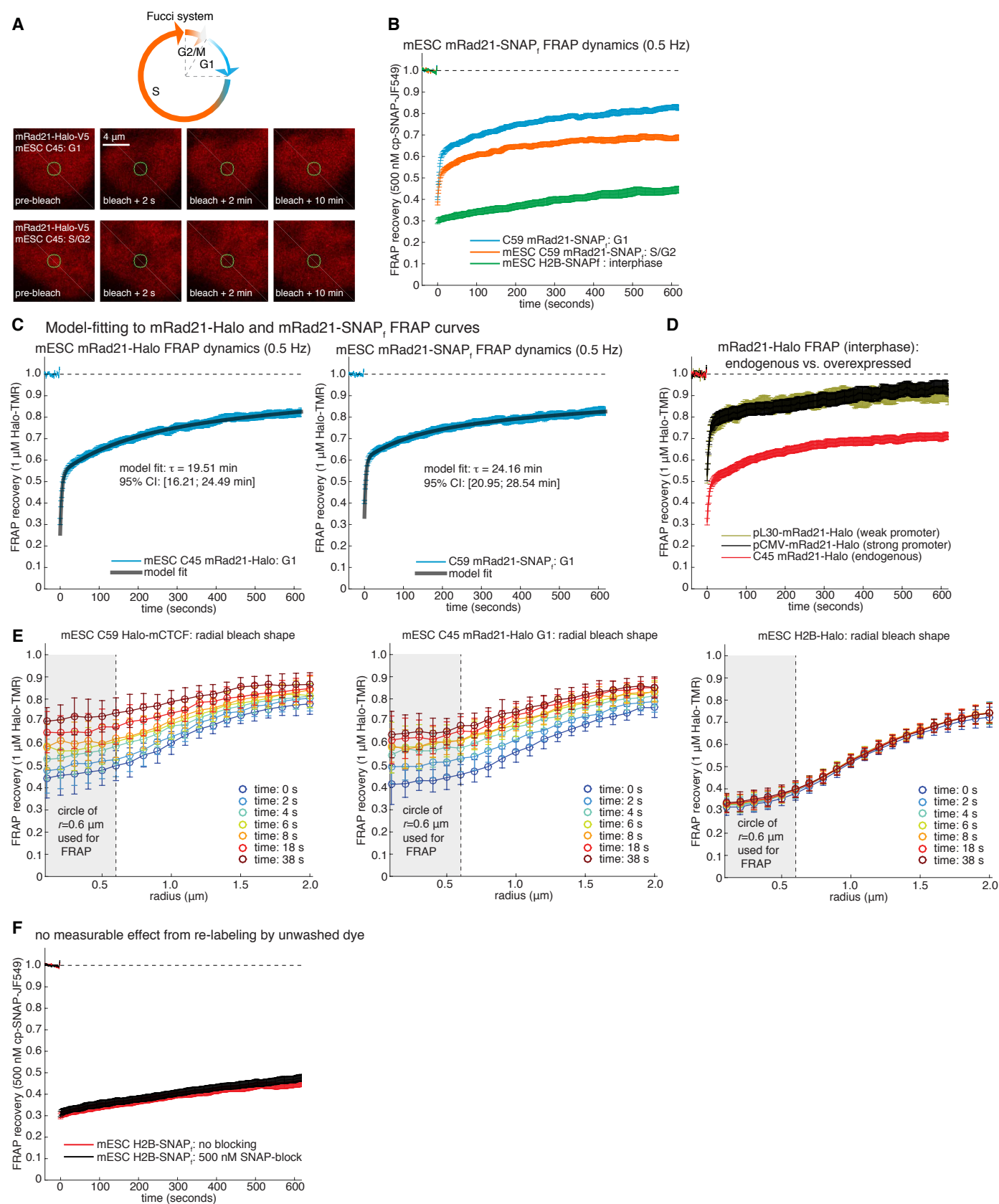


Figure 2 - Figure Supplement 4

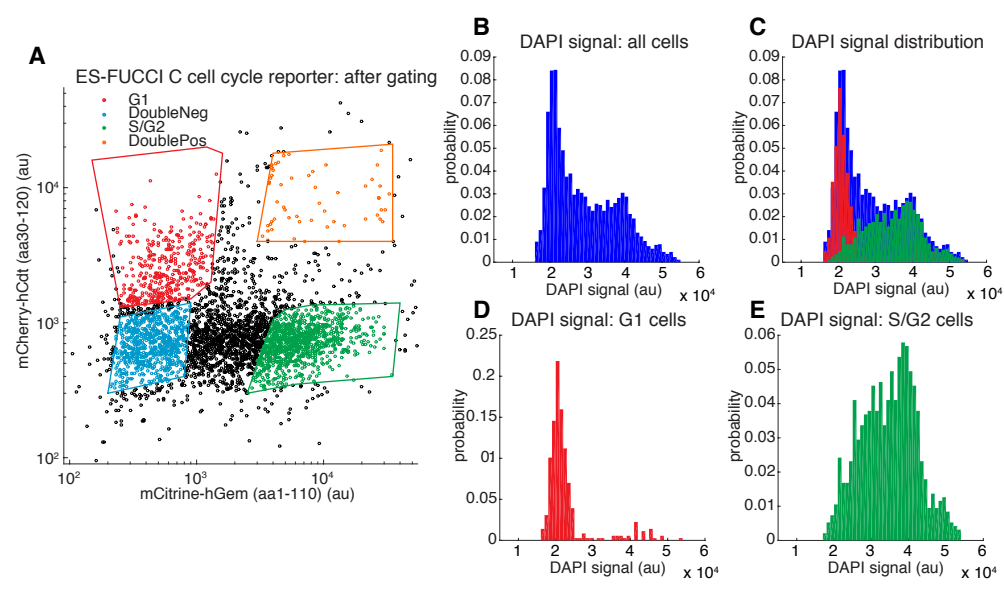


Figure 3

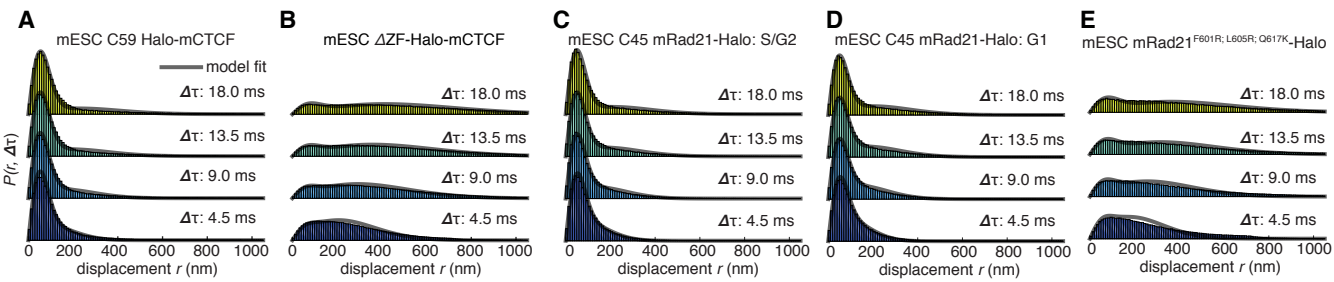


Figure 3 - Figure Supplement 1

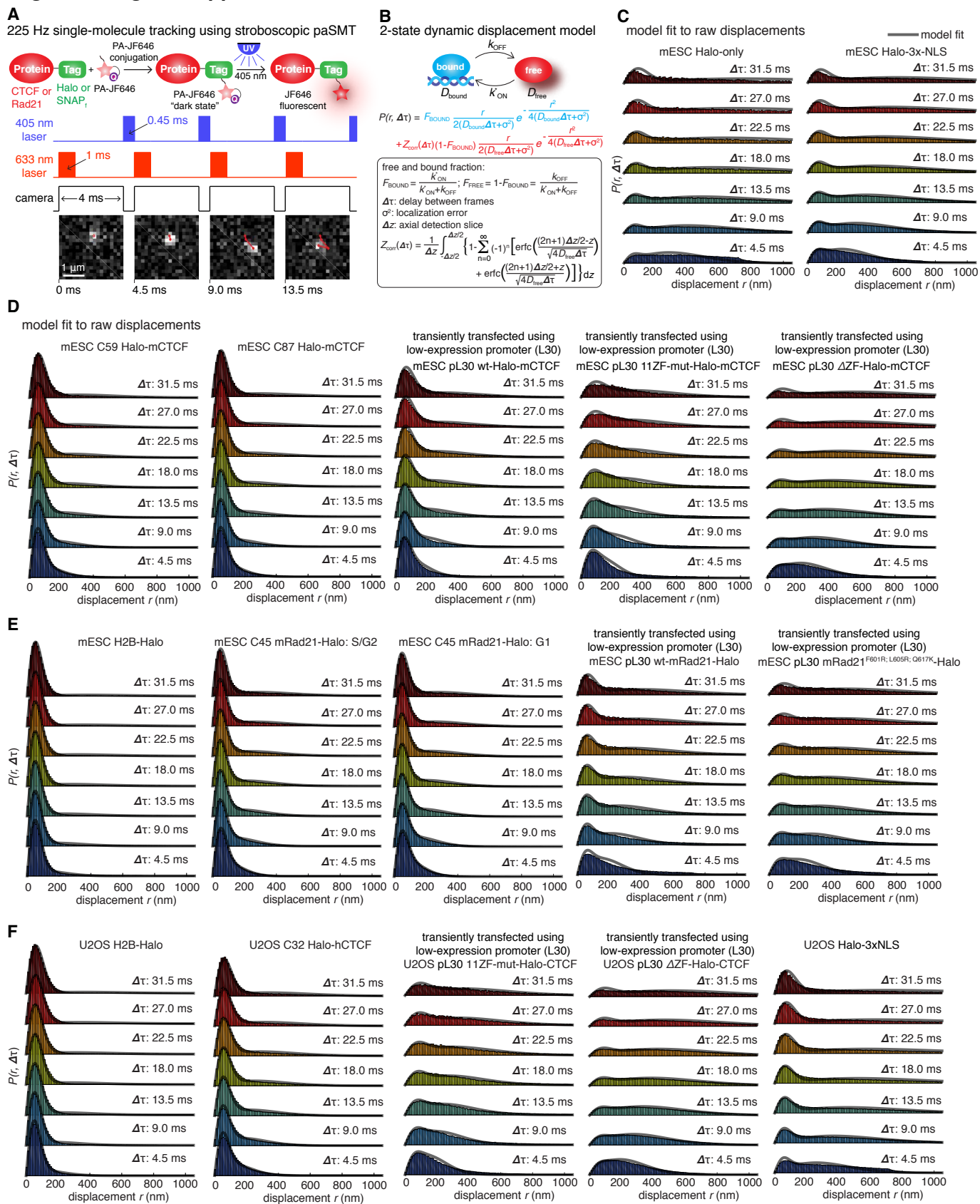


Figure 4

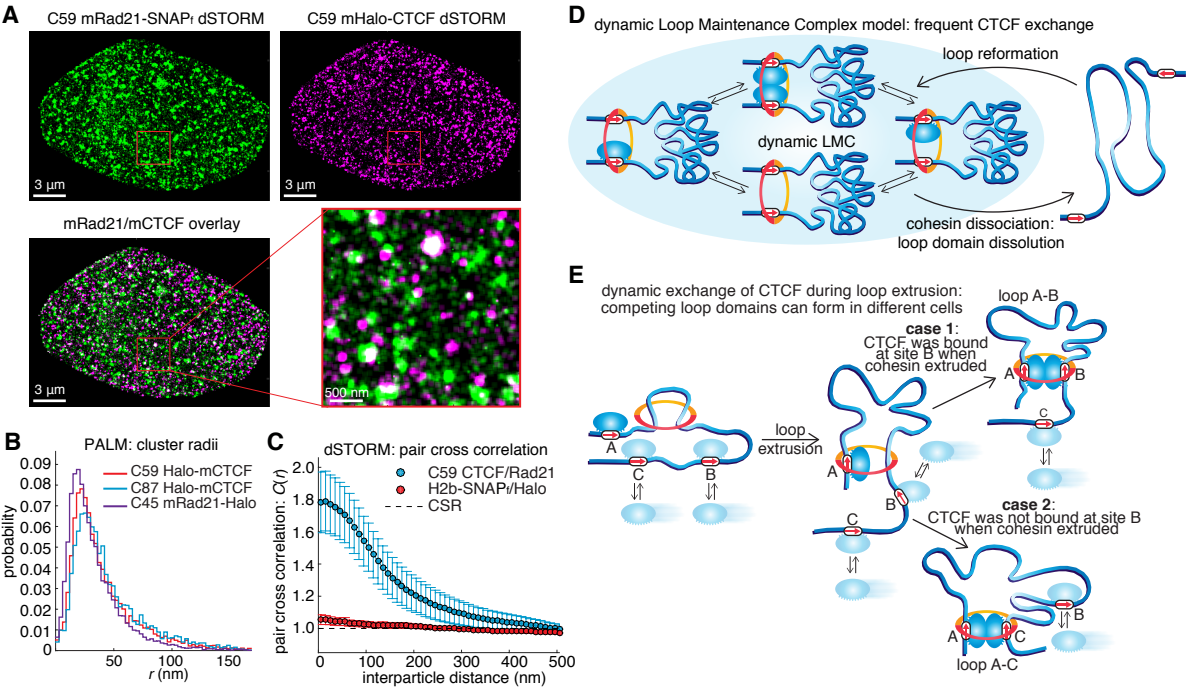


Figure 4 - Figure Supplement 1

